

Fiber Analysis in Micro Structures

Thesis approved by
the Department of Computer Science
University of Kaiserslautern-Landau
for the award of the Doctoral Degree
Doctor of Engineering (Dr.-Ing.)

to

Andreas Grießer

Date of Defense: 11.09.2025

Dean: Prof. Dr. Christoph Garth

Reviewer: Prof. Dr. Hans Hagen

Reviewer: Prof. Dr. Volker Schmidt

Reviewer: Dr. Andreas Wiegmann

DE-386

Abstract

In the last two decades, micro-computed tomography (micro-CT) scanning technology has become affordable and widely available for industrial and research applications. Imaging technology has evolved from requiring synchrotrons for high-resolution images in to desktop scanners providing submicron resolution or 4D dynamic imaging in a lab-based system [1] [2]. This popularized the application of micro-CT scans in material science. Fibers, by nature, have a very high aspect ratio, requiring high resolution to resolve their cross-section while needing enough field of view to capture their trajectory. Extracting properties of the microstructure from micro-CT scans opens up a wide range of possibilities, from comparing different manufacturing methods to creating digital models of the materials [3], [4] and changing them to investigate how specific microstructural properties impact overall performance [5]. A method was developed to analyze the fibers in large micro-CT scans of nonwoven materials [6]–[8]. Nonwoven fibers can be multiple millimeters long, typically in a diameter range of 15-30 micrometers. To overcome typical issues of skeletonization-based approaches, I present a machine learning-based method to find the centerlines of each fiber in the scan. These centerlines are then processed into a graph to correct errors in the neural network’s output. Training data for the neural network was obtained using the structure generator ”FiberGeo” in ”GeoDict”. I demonstrated the approach on a large nonwoven micro-CT. Fiber-based structures like carbon paper also play an important role as gas diffusion layers in fuel cells. Carbon paper is a porous composite made from carbon fibers and carbonized binder. When imaging these materials in a micro-CT, the binder and the fibers do not have any contrast. The distribution of binder and fibers influences the physical properties of the gas diffusion layers. To segment fibers from binder in these images, a machine learning-based approach is presented [9]. Similar to before I created artificial models of carbon paper. For these models, we know which voxels are binder and which are fibers. The models are used to train a neural network that segments the binary images (pore and solid) into three-phase images (pore, fiber, and binder). I presented the approach on multiple scans and also validated it against a small cutout that was labeled manually. For injection-molded composites, the length of the fibers after the injection process can significantly influence the overall strength of the materials[10], [11]. To measure the fiber length, I enhanced the fiber identification method from before with a larger training dataset. I applied our enhanced method to a sample of a glass fiber composite and compared the results to experimental lab measurements. The method presented gave good agreement, enabling the measurement of fiber length without destruction of the sample and the experimental work.

Acknowledgements

The research and writing of this thesis were conducted at Math2Market GmbH and the Computer Graphics and HCI group at the University of Kaiserslautern-Landau.

The work conducted on nonwoven materials in Chapter 2 was conducted in cooperation with Reicofil Reifenhäuser GmbH & Co. KG. I want to thank Michael Mass and Reicofil Reifenhäuser GmbH & Co. KG for letting us use, scan, and analyze their material samples and for their cooperation.

The work conducted on composite materials in Chapter 4 was part of the "DigiLaugBeh" research project (Digital design of a lightweight component - Numerical design of a lye container with regard to service life taking ecological aspects into account)¹, which was funded by the Federal Ministry of Economics and Climate Protection (BMWK) under the funding code 03LB3044C and coordinated by the project management organization Jülich (PtJ). I want to thank the BMWK and all project partners - especially Bosch and the Fh-ITWM - for their close cooperation, exchange and support during the project.

Completing this thesis was a lengthy process that required the support and assistance of many individuals. I want to thank my academic advisor, Prof. Dr. Hans Hagen, who was always available to guide me through this work. I would also like to express my special thanks to my colleagues at Math2Market, particularly Andreas Wiegmann, PhD, Dr. Erik Glatt, and Dr. Rolf Westerteiger. Their academic and technical expertise was invaluable in helping me achieve the results presented in this thesis. I am deeply grateful for the positive and dynamic work environment at Math2Market, which allowed me to perform this work alongside my other responsibilities.

Finally, I want to thank my wife, family, and friends for their constant support and encouragement during this time.

September 24, 2025, Andreas Grießer

¹<https://www.math2market.com/math2market/publicly-funded-projects/digilaugbeh.html>

Contents

Abstract	iii
1. Introduction	1
1.1. Motivation	1
1.2. Related Work	2
2. Identification and analysis of fibers micro-CT scans of nonwoven textiles	5
2.1. Abstract	5
2.2. Introduction	6
2.3. Related Work	6
2.4. Approach	8
2.5. Results	14
2.6. Core Reference	23
3. Segmentation of binder and fibers in gas diffusion layers	25
3.1. Abstract	25
3.2. Introduction	26
3.3. Related Work	27
3.4. Method	29
3.5. Results	34
3.6. Core Reference	41
4. Fiber length determination for injection molded glass fiber reinforced composite materials	43
4.1. Abstract	43
4.2. Introduction	44
4.3. Related Work	44
4.4. Approach	45
4.5. Results	49
4.6. Core Reference	51
5. Conclusion	53
Bibliography	55

A. Curriculum Vitae	65
B. List of Publications	67
B.1. Core publications	67
B.2. Further publications	67

List of Figures

2.1. Centerline labeling: Figure 4.4a shows two fibers cut out from nonwoven sample C. The fibers are parallel and touch each other over a long distance. Figure 4.4b shows the result of labeling the individual fibers with the method presented here. The two fibers are correctly separated. Figure 2.1c shows the extracted fiber centerlines using the neural network approach. In contrast, Figure 2.1d shows the centerlines, as created by skeletonization.	9
2.2. Generated fiber and the corresponding centerline obtained from the analytic model.	10
2.3. Example of fibrous training structure generated with Fiber-Geo [49], including overlap by maximally 2 voxels and added smoothing of fiber contacts to match typical micro-CT scan artifacts (highlighted in the small image).	11
2.4. The adapted 3D U-Net architecture used in this work.	12
2.5. Top: Validation sample 1 to 3. Bottom: Only the wrongly classified fibers, showing 13, 33 and 17 errors respectively from left to right.	14
2.6. Generated validation structure 3 with a solid volume percentage of 11.9% and 339 individual fibers.	15
2.7. Left: ground truth of the validation structure 3 (every voxel is assigned to a fiber). Right: Result of the fiber identification algorithm.	15
2.8. 2D view of validation sample 3 and the fiber identification result. Even the artificially generated noise surfaces are labeled correctly.	16
2.9. All fiber segments with errors in the result of the fiber identification process of validation sample 3. Most errors occur close to the boundary due to boundary error done by the neural network.	17
2.10. 3D and 2D view of Sample C.	18
2.11. 3D and 2D view of Sample B.	19
2.12. Sub-volume of Sample C (2000 by 1000 by 2112 Voxels) with labeled fibers.	20

2.13. Split view of the Segmented Sample C and the labeled fibers colored in different colors.	21
2.14. Split view of the Segmented Sample B and the labeled fibers colored in their individual colors.	21
2.15. Some fibers of Sample B colored. The remaining fibers are rendered transparent.	22
2.17. Orientation analysis of Sample C. The columns on the left show the orientation tensor visualized in the three main planes. . . .	22
2.16. Comparison of the curvature distribution of sample B and C. .	23
3.1. : Four 2D slices of Toray Carbon Paper TGP-H-030 with different amounts of wet proofing (top left: GDL1 5% wet proofing, top right: GDL2 10% wet proofing, bottom left: GDL3 30% wet proofing, bottom right: GDL4 50% wet proofing).	26
3.2. Grey value image and segmented result of the method from this work showing fibers in grey, binder in red and pores in white. .	29
3.3. Example of generated fibers at 10 voxels fiber diameter. Left: no overlap, center one voxel overlap, right: 1 voxel overlap and small amounts of binder added to smooth out the contact. . . .	31
3.4. Example of in-plane slices of training data and real samples. A1: input image for supervised learning A2: output image for supervised learning B1: GDL1 segmented into pore and solid space B2: GDL1 segmentation of binder fibers and pore space using the method from this work.	32
3.5. Visualization of a subset of the 100 artificially generated training samples. All training structures are generated similarly, but key properties like the number of fibers and the amount of binder vary from structure to structure.	33
3.6. Validation datasets: top less binder, bottom more binder; left fewer fibers, right more fibers.	34
3.7. Four color image showing correctly labeled fibers in dark red and correctly labeled binder in dark blue. Fiber material that has been labeled as binder is shown in bright red, and binder that has been labeled as fiber is shown in light blue. A typical error is visible in the top right: A fiber is not traced completely through a bigger binder accumulation.	36
3.8. Left: Manually labeled crop of GDL1. Right: Output from the method presented here.	37
3.9. Four color image showing correctly labeled fibers in dark red and correctly labeled binder in dark blue. Fiber material that has been labeled as binder is shown in bright red, and binder that has been labeled as fiber is shown in light blue. GDL1 with manual labels was used as the ground truth here.	38
3.10. GDL2 after binarization and after applying the method from this work to segment fibers (grey) and binder (red).	38

3.11. Comparison of the amount of fiber and binder material detected in the four samples. Left: Total binder (red) and fiber (blue) percentages. Right: Distribution of fiber (blue) and binder (red) fractions in each z slice.	39
3.12. 2D density projections in the through-plane direction of all samples showing the overall material, only the fiber material, and only the binder material. Color scales have been set to 0 (dark blue) to 1 (red) for all plots.	40
4.1. Rendering of a PP-LGF30 sample after CT scanning and segmentation. This sample will be used for fiber length determination in this work. A section has been cut out to give more detailed insights into the structure.	44
4.2. CT scan before analysis	46
4.3. One example training structure containing a solid volume fraction of 9.1% of isotropically oriented fibers	47
4.4. Example of how the improved neural network performs on glass fibers from a glass wool sample. Figure 4.4c shows a morphological skeleton. Figure 4.4d shows a distance transform-based approach. Both approaches perform worse than the neural network-based approach presented in this work, shown in Figure 4.4e	48
4.5. Identified single fibers in the CT-scan are marked by color coding	49
4.6. Comparison of fiber length distribution obtained from experiment (orange) and digital analysis (blue)	50
4.7. Fiber orientation analysis on a crop of the PP-LGF30 sample. The two images on the top show the orientation in each fiber voxel encoded as the angle to the x-axis. The bottom image shows the three components of the fiber direction averaged for each slice in the z-direction.	50
4.8. Final result of the fiber identification with each fiber labeled in a different color	51

1. Introduction

1.1. Motivation

Micro-structural properties play an essential role in modern porous or composite materials. The geometry of pores and solids in such materials significantly impacts the overall performance of a material towards certain design goals. Engineered materials can be created in various ways. A few examples are: Lay-down of infinite fibers, packing of grains, foaming of polymers or metals, injection molding of fibers and polymer matrix, etc. In many of these processes, fibers are used. Fibers allow a wide range of design options for materials. For example, in composites, their material strength, diameters, and orientation greatly impact the weight and stiffness of the final product. In nonwoven hygiene products, multiple layers of long extruded polymer fibers are often used to design sheets with specific flow properties and fluid holding capabilities. While at least some parameters like the fiber diameters, length, or overall amount can be controlled on the input side of many production processes, some other properties can not be controlled or might even be changed by the process. Understanding the final geometry and distribution of fibers in the produced material can be an important tool in understanding the processes that control the overall performance of a material [5].

In the last two decades, micro-computed tomography (micro-CT) scanning technology has improved rapidly and has become more available for material engineering. In the early 2000s, the availability of micro-CT devices was very limited, and often scanning materials with fibers in the micrometer range at a sufficiently large field of view and quality required a synchrotron. On top of this, processing the large volumes produced by these scans can now be done on commonly available workstations. By now, lab-based systems can even be used to capture dynamic processes such as deformations under load [2] or even tracing particles in a fluid under limited conditions [1]. These progresses has also caused increased demand for tools to obtain not only qualitative but also quantitative insights from micro-CT scans. For fiber-based materials, the microstructure can be very complex, and the quantification of geometrical properties is not easy. For some properties like orientation of fibers [12], diameters of fibers, or pore sizes, image-based approaches exist that yield reliable results. To fully describe the material's microstructure, it is necessary to separate the individual fibers and describe them analytically. In Chapter 2 of this work, I present a solution to this challenge that labels the individual fibers in nonwoven materials. The samples that were analyzed are materials typically used in hygiene products. In these samples, the curliness and curvature of fibers were of high interest. In Chapter 4, this method is further

improved for the challenges imposed by the high density of fibers typically observed in composite materials. Here, the fiber length distribution after the sample production was of interest and can easily be computed from the analytic representations of fibers constructed by the approach presented in this work.

Many materials are not composed solely of fibers; they often include a blend of fibers and other components, such as grains (e.g., super absorbent particles) or binders that hold the fibers together, providing the necessary mechanical stability. One such type of material is carbon paper, which consists of carbon fiber glued together by a carbonized binder material. Carbon papers are often used as gas diffusion layers (GDL) in fuel cells and play an essential role in the overall performance of the fuel cell. The amount of binder and its distribution are critical design parameters. In micro-CT scans, the binder and the fibers usually do not have any contrast and can not easily be segmented into different phases. To overcome this challenge, I developed a method to segment fiber and binder using a convolutional neural network trained on artificially generated samples in Chapter 3. This method allows the analysis of fiber and binder distribution in carbon paper materials. Further, the proper constituent material properties can be assigned and used for simulation of e.g., conductivity.

Both the characterization of phase distribution and the geometric description of objects making up the microstructure yield important inputs for modeling of this kind of material [3], [4]. Generating accurate models from such measurements of scans of the real materials can be used to design materials according to certain criteria. With modern simulation tools, the design of materials can be optimized towards certain goals without the need to produce and test each sample in a lab. This helps to achieve goals faster while being more sustainable.

1.2. Related Work

A wide range of methods to analyze the characteristics of fibers in microstructures was developed in the past. Some approaches do not require the identification of individual fibers and instead use image-based methods. E.g., Axelsson et al. [12] focus on the computation of fiber orientation. They calculate the structure tensor in each voxel of a 3D image and use the eigenvalue decomposition to determine the local fiber orientation. Krause et. al. [13] Determine the fiber orientation by minimizing a quadratic energy functional, which is smoothed using a Gaussian. These methods all work directly on the image without labeling individual fibers. Another approach to measuring fiber length in micro-CT scans that does not rely on single fiber identification is presented by Kroneberg et al. [14]. They detect fiber endpoints based on the surface curvature and then use them to estimate the fiber length based on an approach presented by Kuhlmann and Redenbach [15]. This method is limited to straight fibers only.

More similar in methodology to my work, Henyš et. al.[16] segment indi-

vidual fibers of woven materials and yarns. Instead of using neural networks, they obtain the fibers from a skeletonization approach. The skeleton is decomposed into segments that are reconnected afterward. The approach works well for micro-CT scans where the resolution allows the distance map-based skeletonization to separate the centerlines of touching fibers. Huang et al. [17] use a similar technique with a different skeletonization approach which preserves the original topology. They then use a heuristic to separate the wrongly connected fibers at junction points based on correlating the length of skeleton segments to the fiber diameters.

Viguié et al. [18] describe a method to identify individual fibers by analyzing the fiber orientation to detect zones with high orientation gradients in their work. This method works well for various kinds of materials. However, parallel fibers (as in composite materials) require additional steps to achieve a segmentation, as no gradient can be observed. Badran et al. [19] present a method to segment phases by shape in micro-CT scans that have no contrast using deep learning.

Depriester et al. [20] remove contact points between fibers by measuring the local misorientation of fibers. The resulting fiber fragments were then reconnected using an orientation-based growth algorithm. The method works well for fibers not primarily parallel and in contact over long distances, where reconnecting them will become problematic. Konopczyński et. al. [21] present an approach where a deep fully convolutional network calculates a mapping of the fiber voxels in an embedding space. This embedding is later clustered to obtain the segmentation of the individual fibers. The method works well for the low-resolution micro-CT scans demonstrated, but is limited by the requirement for manually labeled training data. Other commercial solutions for the analysis of fibers in fiber-based materials are available, such as "Avizo" [22]. These approaches solve the problem of analyzing geometrical properties for a particular parameter (e.g., orientation) or certain types of structures. Kallel et. al. [23] present an algorithm to create artificial fiber structures and simulate thermal conductivity on these samples.

More basic but similarly crucial to analyzing the fibers is getting the actual phase distribution right for materials that contain more phases than just fibers and air or matrix material.

For the segmentation of material phases (semantic segmentation) in micro-CT scans, many machine learning approaches exist and have been deployed successfully. One example is the trainable WEKA segmentation [24]. This approach uses manual labeling on 2D images to obtain training data. However, manual labeling of images is very time-consuming. It is also error-prone, with results depending heavily on the expertise and experience of the user. Another notable approach using deep learning for segmenting minerals in rocks is by Phan et. al.[25], who train an improved U-Net architecture to segment pores and minerals on micro-CT scans of rock samples. They start from high-quality scans of multiple rock samples, segment each using existing segmentation methods, and enhance this training dataset with artificially added artifacts. A similar process on a single rock type is presented by Karimpouli

et al. Al. [26]. Our approach differs from these methods by generating the training data completely from models, using 3D fiber and binder modeling tools available in the GeoDict software [27]. Deep learning-based approaches to segment GDLs have also been used by Tang et al. [28] and Mahdaviara et al. [29]. In both works, a segmentation of binder and fiber similar to this work is achieved. In contrast to the work presented here, they start from scans in which there is a contrast in grey values between binder and fibers. This contrast allows the creation of training data for the deep-learning part by semi-automatic tools. There have also been attempts to segment binder and fiber using classical approaches. One such approach is presented by Chen et al. [30], who use a multi-threshold non-local means joint distribution method to find the distribution of fibers and binder. In contrast to our approach, they also require a difference in grey values between fibers and binder for the approach to work. The binder modeling approach presented in this work is similar to the approach presented by Simaafrookhteh et al. [31], who create the binder phase in 3D scans of GDLs using morphological operations. They also investigate the effect of different amounts of binder on carbon paper's permeability, diffusivity, and thermal conductivity. The same approach of adding binder by morphological operations to investigate the effects on performance has been used for batteries by Hein et al. [32] and Trembacki et al. [33]. Similarly, Wang et al. [34] investigate the impact of hydrophobicity on the water transport velocity of Toray GDLs. Their approach alters the GDLs by adding hydrophobic decorations on top and bottom, changing morphology and fiber diameters, and increasing the breakthrough pressure. More work on the impact of the amount of binder on the performance of a GDL has been done by Flückiger et al. [35]. They experimentally studied different binder amounts and PTFE treatments on GDLs and concluded that binder amounts over 50% negatively impact effective diffusivity. Yiotis et al. [36] study the influence of binder on the performance of a GDL by generating models using the same approach to create the fiber network as used in this work. Investigating the performance of GDLs and other parts of fuel cells by simulation has been an approach adopted in many works, for example Zamel et. al. [37], Hrandi et. al. [38] or Simaafrookhteh et. al. [31]. For these works, it is beneficial to obtain a separation of the fiber and binder phases in micro-CT scans of GDLs to account for their different physical properties in simulations. Our approach models GDLs as training data for a neural network in a two-step process. First, a fibrous structure is created using a Poisson line process. Then, the binder distribution in the fiber structure is simulated using morphological operations. The basic idea of the first step is described by Schladitz et. al. [39]. Straight, infinitely long, potentially overlapping fibers are generated from a Poisson line process according to an anisotropic direction distribution and a given fiber diameter distribution. This approach gets statistically correct fiber distributions in finite-sized domains. The approach is extended by moving and bending the fibers after the initial creation to allow the fibers to overlap only a defined amount.

2. Identification and analysis of fibers micro-CT scans of nonwoven textiles

Contents

2.1. Abstract	5
2.2. Introduction	6
2.3. Related Work	6
2.4. Approach	8
2.4.1. Fiber centerlines	8
2.4.2. Identification of centerlines by neural networks	8
2.4.3. Training data generation	9
2.4.4. Neural Network	11
2.4.5. Centerline to graph conversion	12
2.4.6. Fragment reconnection	12
2.4.7. Graph to Analytical Fiber	13
2.4.8. Fiber analysis	13
2.5. Results	14
2.5.1. Synthetic Data	14
2.5.2. Real Data	18
2.5.3. Conclusion	23
2.6. Core Reference	23

2.1. Abstract

Fibrous materials play a significant role in many industries, such as lightweight automotive materials, filtration, and as constituents of hygiene products. The properties of fibrous materials are governed to a large extent by their microstructure. One way to access the microstructure is to use micro-computed tomography (micro-CT). Completely characterizing the microstructure requires geometrically characterizing each individual fiber. To make this possible, one must identify the individual fibers. The method presented in this work achieves this by finding the centerline of all individual fibers in segmented micro-CT scans. It uses a convolutional neural network trained on automatically generated synthetic training data. From the centerlines, analytic descriptions of the individual fibers are constructed. These analytic representations

allow detailed insights into the statistics of the geometric properties of the fibrous material, such as the fibers' orientation, length, or curvature. The method is validated on artificial data sets and its usefulness demonstrated on a very large micro-CT scan of a nonwoven composed of long fibers with random curvature.

2.2. Introduction

Fibrous materials play a significant role in many industries, such as lightweight automotive materials [40], [41], or as constituents of hygiene products [42]. Because the details down to the individual fibers govern the material properties, understanding the microstructural geometric statistics of fibrous materials is an essential aspect of material engineering. Analyzing fibers has therefore been of interest to researchers for a long time. First, besides manual measurements, 2D image analysis was used for this task [43]. In the last 15 years, volumetric 3D scanning technology such as micro-CT has become affordable and widely available, popularizing its application for the analysis of nonwovens [44], [45]. 3D scans can provide valuable insights into materials under two constraints: The scanning resolution must be sufficient to resolve all relevant objects and features, and the field of view must be large enough to be statistically relevant for the material under consideration. In recent years, both fiber analysis and the generation of artificial models of fibrous structures have become an important research topic [46]–[48]. Correct labeling of fibers in a 3D scan allows for the complete characterization of the geometric properties of each fiber and, subsequently, of the statistical properties of the whole material sample. Depending on the application domain, the fibers can look vastly different. For example, composite materials use densely packed straight fibers, while nonwoven materials consist of highly curved fibers with a low packing density. This diversity poses a challenge when developing a generic algorithm. The algorithm must also be efficient enough to analyze large micro-CT scans that capture a field of view representative of the material to characterize it accurately. To obtain valuable insights, the algorithm must perform on large 3D micro-CT scans, which capture a large enough field of view of the material, a so-called representative elementary volume (REV).

2.3. Related Work

A wide range of methods to analyze the characteristics of fibers was developed in the past. Some approaches do not require the identification of individual fibers and instead use image-based methods. Axelsson et al. [12] focuses on the computation of fiber orientation. They calculate the structure tensor in each voxel of a 3D image and use the eigenvalue decomposition to determine the local fiber orientation. Krause et al. [13] determine the fiber orientation by minimizing a quadratic energy functional, which is smoothed using a Gaussian. These methods all work directly on the image. In contrast to that approach, I identify the individual fibers and find analytic representations for them.

This representation consists of a piecewise linear trajectory and cross-sectional parameters. In the simplest case of fibers with constant circular cross-sections, the latter is the diameter. The fiber orientation can then be calculated from the analytic representation.

More similar in methodology to my work, Henyš et. al.[16] segment individual fibers of woven materials and yarns. Instead of using neural networks, they obtain the fibers from a skeletonization approach. The skeleton is decomposed into segments that are reconnected afterward. The approach works well for micro-CT scans where the resolution allows the distance map-based skeletonization to separate the centerlines of touching fibers. Huang et al. [17] use a similar technique with a different skeletonization approach, which preserves the original topology. They then use a heuristic to separate the wrongly connected fibers at junction points based on correlating the length of skeleton segments to the fiber diameters.

In their work, Viguié et al. [18] describe a method to identify individual fibers by analyzing the fiber orientation to detect zones with high orientation gradients. This method works well for various kinds of materials. However, parallel fibers (as in composite materials) require additional steps to achieve a segmentation, as no gradient can be observed. In their work, Badran et al. [19] present a method to segment phases by shape in micro-CT scans that have no contrast using deep learning.

Depriester et al. [20] remove contact points between fibers by measuring the local misorientation of fibers. The resulting fiber fragments were then reconnected using an orientation-based growth algorithm. The method works well for fibers that are not primarily parallel and in contact over long distances, where reconnecting them will become problematic. Konopczyński et. al. [21] present an approach where an embedding of the fibers is calculated by deep learning. This embedding is later clustered to obtain the segmentation of the individual fibers. The method works well for the low-resolution micro-CT scans demonstrated, but is limited by the requirement for manually labeled training data. Other commercial solutions for the analysis of fibers in fiber-based materials are available, such as Avizo [22]. These approaches solve the problem of analyzing geometrical properties for a particular parameter (e.g., orientation) or certain types of structures.

A limiting factor of machine learning-based approaches for fiber segmentation is often the time-consuming work it takes to manually label enough volumetric data to train the neural network. The approach presented here avoids this problem by generating synthetic training data automatically using the fiber generator software "FiberGeo" [49] in "GeoDict" [50]. The training data can be easily adapted by modifying the generator parameters to resemble many different types of fibrous materials.

Like the method presented here, artificially generating fiber structures for training, Kallel et. al. [23] present an algorithm to create artificial fiber structures and simulate thermal conductivity on these samples. Constructing the analytic fiber models allows for the straightforward computation of various properties. Statistics over those geometric properties enable the creation of

accurate models of the analyzed material [4] [3]. At the same time, the method presented is efficient enough to be applied to scans of industrial dimensions. At this scale, the statistics can be used to determine material properties relevant for patents and patent claims (Patent No. WO 2020/103964 A1, 2020 [51]).

2.4. Approach

The method presented here starts on segmented (binarized) micro-CT images. These images classify each sample point (voxel) as being either part of the background/matrix (0) or part of a fiber (1). Starting with segmented images makes the method very flexible regarding the segmentation algorithm and robust against the various artifacts that can occur in gray value scans from micro-CTs. Much research has been done on segmenting micro-CT images, and a suitable method can be chosen depending on the type of analyzed material.

2.4.1. Fiber centerlines

Each fiber trajectory is described using its centerline, a piecewise linear curve along the center of each fiber. Additionally, the fiber's local diameter is stored at each centerline point. For non-circular fibers, a different shape descriptor can be chosen - e.g., the two diameters of an ellipse for fibers with an elliptical cross-section. In the approach presented here, I label each fiber's center voxels to obtain a discrete representation of the centerline as a connected component of voxels. Then the algorithm traces along these voxels to obtain an analytical representation. Finding the centerline of a fiber is challenging in areas where fibers touch or are melted together, as can happen in the case where the material is thermally bonded.

2.4.2. Identification of centerlines by neural networks

A natural approach to obtaining the discrete centerlines is skeletonization. Here, a binarized voxel image is selectively eroded until only a discretized curve with a thickness of a single voxel remains. However, because skeletonization is topology-preserving, it alone cannot entirely separate fibers that touch in the binarized image (see Figure 2.1).

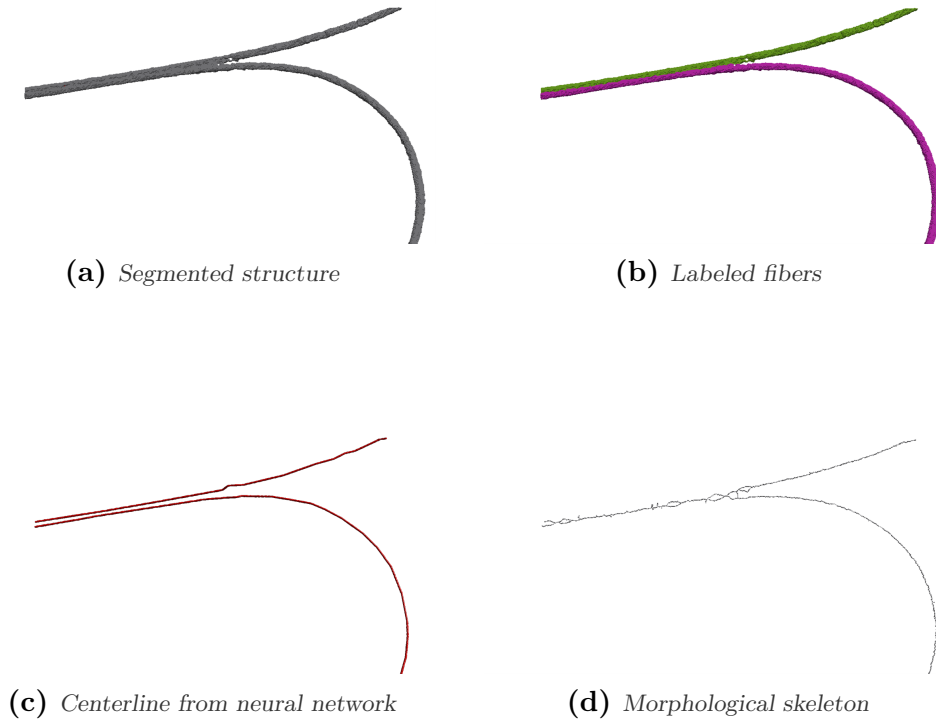


Figure 2.1.: Centerline labeling: Figure 4.4a shows two fibers cut out from non-woven sample C. The fibers are parallel and touch each other over a long distance. Figure 4.4b shows the result of labeling the individual fibers with the method presented here. The two fibers are correctly separated. Figure 2.1c shows the extracted fiber centerlines using the neural network approach. In contrast, Figure 2.1d shows the centerlines, as created by skeletonization.

Unfortunately, this occurs quite frequently, either as an artifact of segmentation or because the fibers are physically connected, as in the case of thermally bonded materials. To avoid this problem, the presented method uses a neural network-based method to find the centerlines of fibers. The neural network labels voxels through which the centerline of a fiber passes in the image, which results in an image similar to skeletonization but without cross-linking neighboring fibers at contact points.

2.4.3. Training data generation

Labeling fiber centerlines manually would be very time-consuming. Therefore, to obtain the necessary training data, I use synthetic models generated from the "FiberGeo" [49] fiber generation module, which is a component of the "GeoDict" [50] digital material laboratory. In these models, the analytic description of the fibers is available, and voxels containing the analytic centerline can be labeled easily (see Figure 2.2).



Figure 2.2.: *Generated fiber and the corresponding centerline obtained from the analytic model.*

For the model to be applicable to real material scans, the synthetic fiber structures used during training should resemble the real materials, at least locally. A wide range of varying fiber structures can be generated quickly by sweeping through the parameters of the fiber generation module "Fiber-Geo" [49]. This approach allows for the obtaining of plenty of training data in a timely manner. It avoids one of the main limitations of supervised learning approaches, the scarcity of training data.

I generated curved fibers several times longer than the domain under consideration for the examples shared later in the results. The curvature was modeled so that both straight and curved segments were obtained. The fibers were mainly oriented in a plane, but a small amount of perpendicular deviation was permitted. Apart from the fiber trajectories, the contact points where fibers touch each other require particular attention. I applied morphological closing to match the appearance of these contact areas to the real micro-CT scans.

As the regions without fiber contacts proved easy for the network to label, I used training structures with an artificially high number of contact points such that these more complex configurations occur more frequently. This was done by simply increasing the density of fibers beyond the density found in the real materials, which naturally leads to more fiber contacts. To train the network, I generated nine artificial fiber structures with 512 by 512 by 256 voxels each (Figure 2.3).

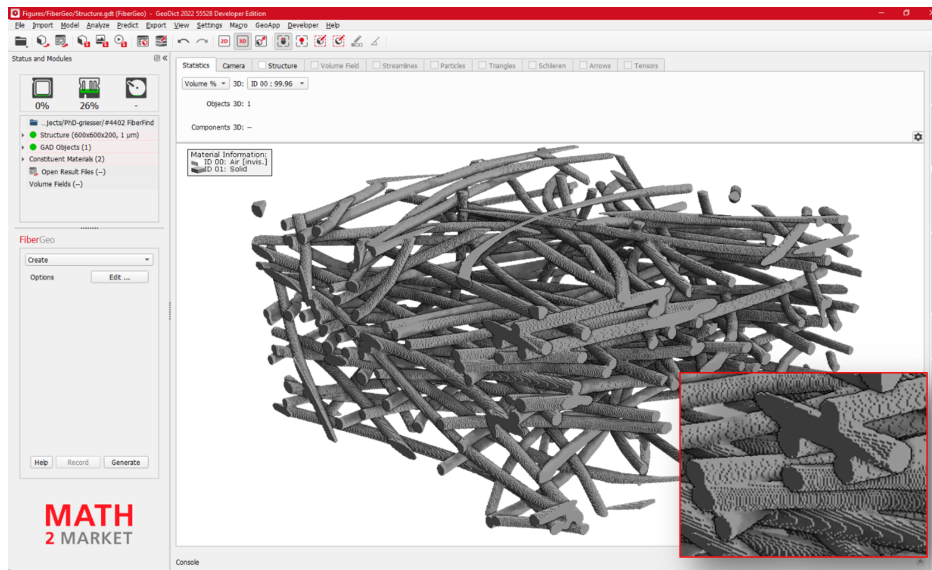


Figure 2.3.: Example of fibrous training structure generated with FiberGeo [49], including overlap by maximally 2 voxels and added smoothing of fiber contacts to match typical micro-CT scan artifacts (highlighted in the small image).

2.4.4. Neural Network

To avoid being limited to fixed image sizes, the neural network is not applied to the whole image all at once. Instead, a sliding input window is passed over the image, and the neural network generates labels for a smaller output sub-window in the center. Because the neural network "sees" only the contents of the input window, that window needs to be large enough to capture the fibers' shape and local trajectory. TensorFlow [52] is used for the deep learning part of the algorithm. As a network architecture, I choose a variation of the widely used U-Net [53] (see Figure 2.4). Presented initially to label 2D microscopy images, I extend the network to a 3D architecture [54]. The network, therefore, transforms a fixed-size 3D input volume to a smaller 3D output volume, which contains the predicted labels for the center region of the input. I train the neural network using supervised learning. This means that inputs and corresponding outputs are passed to the training algorithm. The network learns how to transform the input into the corresponding output using gradient descent optimization. Using a 3D network architecture instead of a 2D slice-based approach comes at the cost of longer training times and a demand for more training data. The latter is largely irrelevant in the approach presented here, as the amount of training data that can be generated is practically unlimited, and the time for data generation is negligible with respect to the training time. The benefit of using the 3D U-Net lies in the quality of the results achieved. A smooth and flicker-free result is generated by considering a 3D context bigger than the network's output size. To keep

the size of the input window and the training times manageable, I reduced the depth of the U-Net to two. Still, I designed the training framework so window sizes and network depth can be adjusted freely, up to the GPU memory limit.

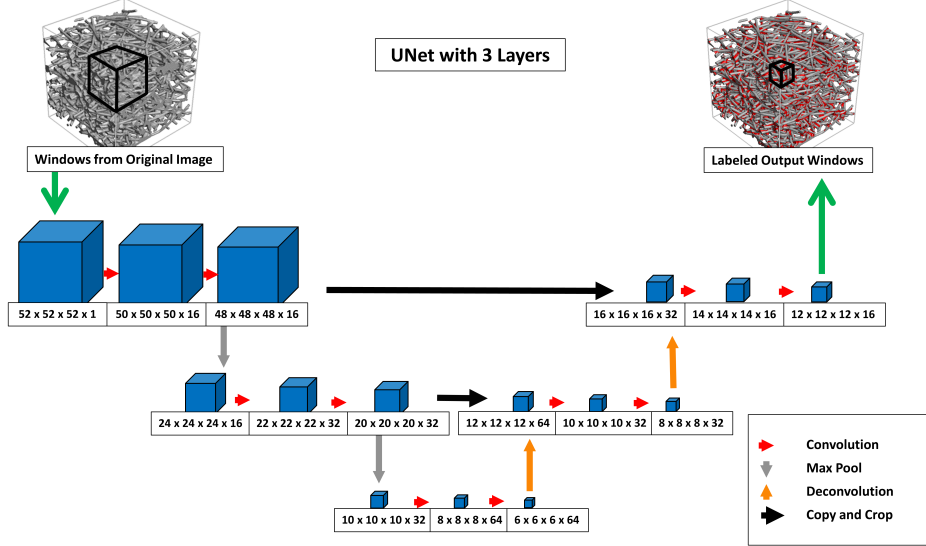


Figure 2.4.: The adapted 3D U-Net architecture used in this work.

2.4.5. Centerline to graph conversion

Applying the network to a segmented scan results in labeled centerlines about three voxels in diameter. I further reduce the diameter to a single voxel by applying a skeletonization algorithm. These chains of adjacent voxels are then converted into a graph representation by starting at the end of a chain and tracing along the neighboring labeled voxels. Ideally, this yields a completely disconnected graph where every fiber is represented as two graph nodes connected by a single edge. The nodes correspond to the endpoints of the fiber, while the edge corresponds to the fiber trajectory. However, this might not be the case due to artifacts in the CT-scan or detection errors in the neural network. Some fibers might fall apart into multiple graph components, and therefore, I use a reconnection step to merge fiber fragments back together. The opposite case of fibers merging is a significant problem in skeletonization-only approaches. However, in the method presented here, this artifact does not occur frequently because fibers in the training data are guaranteed not to overlap so much that the centerlines touch; hence, the output inherits this property for real micro-CT scans.

2.4.6. Fragment reconnection

To reconnect the fiber fragments, I consider all pairs of fragment endpoints that are closer than a specific distance. I define Euclidean length l_{ik} as the distance between two fiber endpoints, and d_i , d_k , and d_{ki} as the directions of the fiber segments and the directions of the segment between the endpoints.

For each endpoint combination, an optimization criterion o_{ik} is calculated. Different optimization criteria are used for straight or curved fibers, and Equation 2.1 is used for primarily straight fibers, and Equation 2.2 is used for curved fibers.

$$o_{ik} = \frac{l_{ik}}{l_{max}} \cdot d_i \cdot d_k + \left(1 - \frac{l_{ik}}{l_{max}}\right) \cdot (d_i \cdot d_{ik} + d_k \cdot d_{ki}) \quad (2.1)$$

$$o_{ik} = d_i \cdot d_k + d_i \cdot d_{ik} + d_k \cdot d_{ki} \quad (2.2)$$

The pair of fragments with the highest value for o_{ik} are then connected (replaced by a single fragment) through interpolation to form a single fragment. I continue with the next best pair in a greedy strategy until no pair of endpoints with o_{ik} larger than a given threshold remains. At the end of this procedure, all fibers in the scan are represented by a list of voxel coordinates connecting the start and end points.

2.4.7. Graph to Analytical Fiber

This list of voxel coordinates is converted into a piecewise linear fiber centerline by merging connections between two voxels so that the resulting line never deviates further than two voxels. This ensures that the noisy nature of the voxelized centerline is smoothed out, but the resulting centerline stays close to the actual position of the fiber. Then, the local diameter at each centerline point is determined by sampling the Euclidean distance map of the segmented CT-scan. In addition to obtaining the analytic fiber representations, I uniquely assign each fiber voxel in the original segmented scan to a fiber. For this purpose, I construct an object-label image where each voxel of a fiber's centerline is assigned a unique ID corresponding to the fiber. Then, a watershed [55] algorithm is used to completely label the fiber voxels surrounding the centerline with that same ID. After this procedure, every solid voxel has the unique ID of the fiber it belongs to. Finally, I calculate the length, orientation, curvature and curl-index [56], [57] of each fiber based on its analytic representation.

2.4.8. Fiber analysis

The curvature of a fiber at a certain point is defined as the inverse of the radius of the tangential circle to the centerline. The fiber curl-index is the ratio between the curve length of the fiber and the Euclidean distance between the two fiber endpoints. In order to analyze the sample for gradients or inhomogeneities with respect to any of the computed properties, I can restrict the analysis to a sub-region of the sample domain. Additionally, it is possible to select a subset of fibers that fulfill a certain criterion and analyze only that subset for other properties (e.g., only analyze fibers above a particular length for curl-index as short fibers that intersect the domain boundary would skew the result). All algorithm steps are implemented with the option to use periodic boundary conditions to analyze unit cells of regular meshes (e.g., woven

fabrics).

2.5. Results

2.5.1. Synthetic Data

	Validation 1	Validation 2	Validation 3
Number of Fibers	221	407	339
Solid Volume Percentage / (%)	9.4	10.8	11.9
Fiber Diameter / (μm)	16-19	13-16	13-16
Noise Artifacts	Yes	No	Yes

Table 2.1.: Overview of the most important parameters for generating the validation samples.

To validate that the approach presented in this work can identify individual fibers, I created three additional synthetic structures for which the ground truth is known (Figure 2.5).

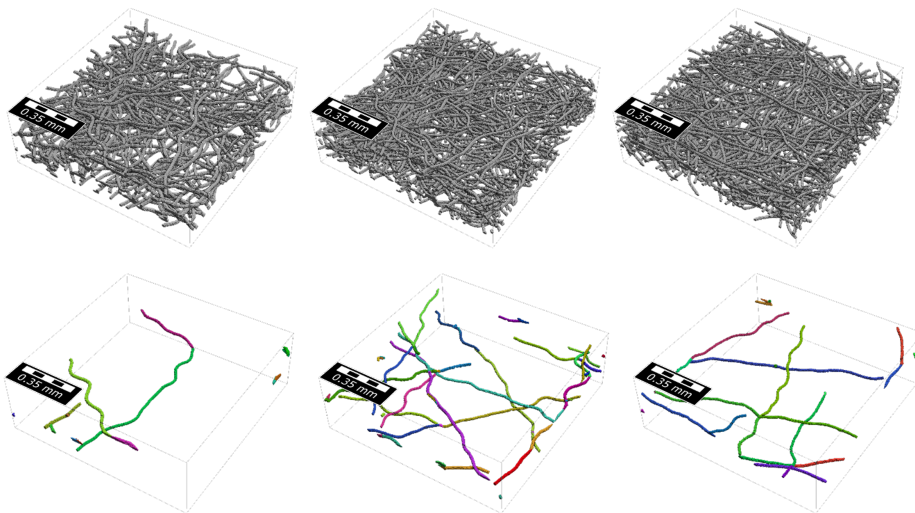


Figure 2.5.: Top: Validation sample 1 to 3. Bottom: Only the wrongly classified fibers, showing 13, 33 and 17 errors respectively from left to right.

The samples were created using "FiberGeo" with the parameters listed in Table 2.1.



Figure 2.6.: *Generated validation structure 3 with a solid volume percentage of 11.9% and 339 individual fibers.*

The fibers were allowed to overlap by $2\ \mu\text{m}$. The voxel length of the generated model is $2\ \mu\text{m}$. A small amount of binder was added to smooth out the contact points of fibers, making the model look closer to a micro-CT scan. On top of this, in Validation Samples 1 and 3, stochastic noise was added to the surface of the fibers to simulate noise in the micro-CT-scan (Figure 2.6).

In contrast to the training data, the fibers were generated slightly elliptical to simulate deformations that might happen during the manufacturing process and test how well the model generalizes to these cases.

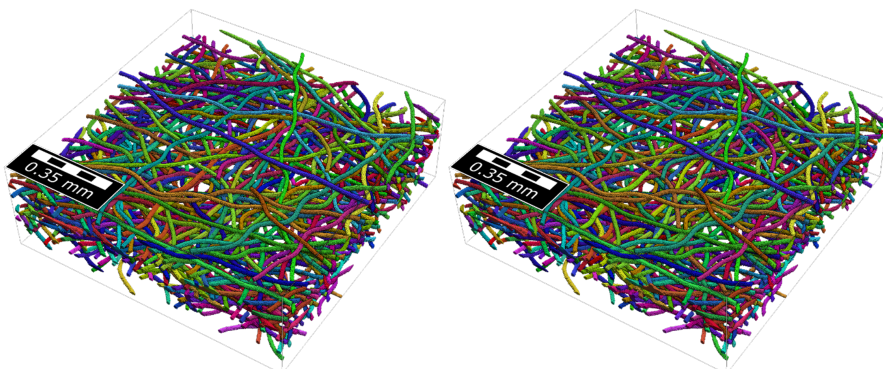


Figure 2.7.: *Left: ground truth of the validation structure 3 (every voxel is assigned to a fiber). Right: Result of the fiber identification algorithm.*

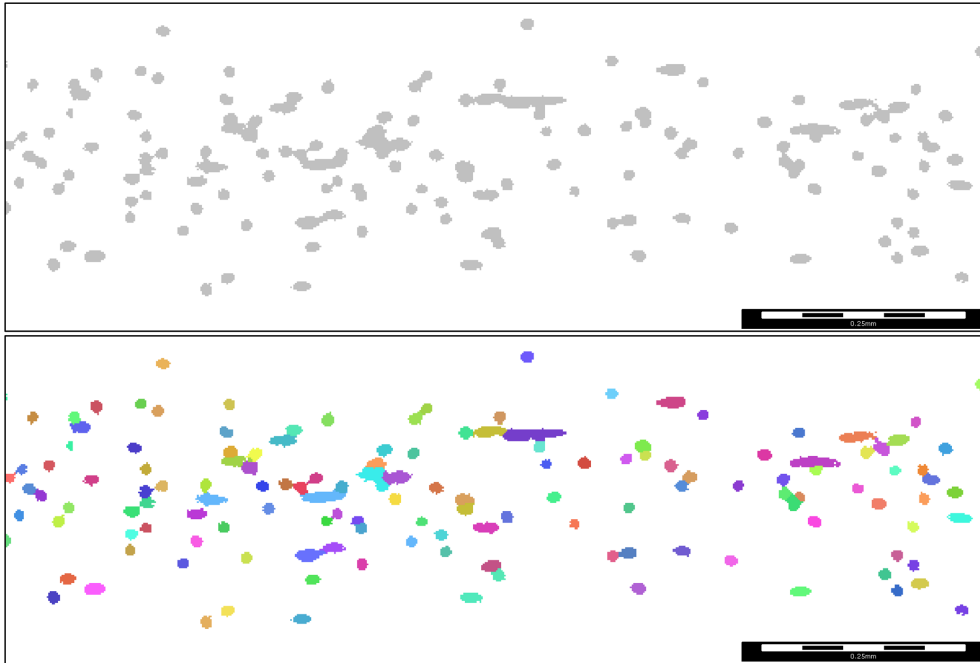


Figure 2.8.: 2D view of validation sample 3 and the fiber identification result. Even the artificially generated noise surfaces are labeled correctly.

The results (see Figure 2.7 and Figure 2.8) were inspected (see Figure 2.9), and the following four types of errors were observed:

1. Boundary Artifacts: Due to the neural network always considering a localized window of $44 \times 44 \times 44$ voxels, errors in the centerline detection can occur near the boundary.
2. Fiber split: In some cases, fragmented fibers are not reconnected by the reconnection algorithm and a fiber may fall apart.
3. Fiber contact error: When fiber centerlines fall apart at a contact point, the fiber reconnection algorithm sometimes connects the wrong fiber ends because they exhibit similar distances and orientations as the correct pairing.
4. Fiber merge: When the endpoints of 2 fibers are close, the algorithm can wrongly merge them into one fiber in some cases.

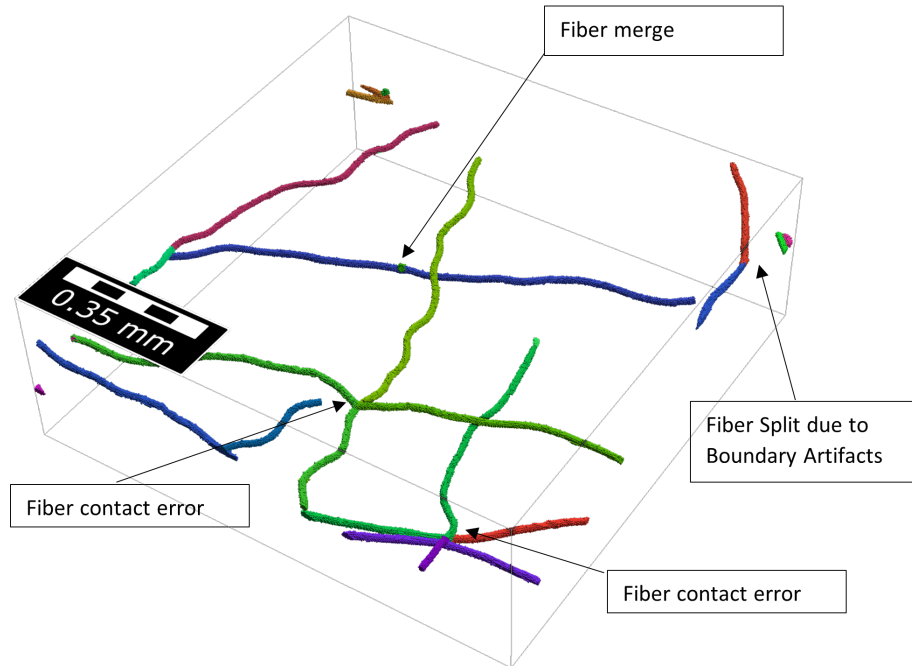


Figure 2.9.: All fiber segments with errors in the result of the fiber identification process of validation sample 3. Most errors occur close to the boundary due to boundary error done by the neural network.

I evaluated the occurrences of these errors for each of the 3 validation samples (Table 2.2).

	Validation 1		Validation 2		Validation 3	
	Absolute	Relative	Absolute	Relative	Absolute	Relative
Number of fibers	221		407		339	
Boundary artifacts	11	5%	20	4.9%	12	3.5%
Fiber contact errors	0	0%	9	2.2%	5	1.5%
Fiber merges	2	1%	4	1%	0	0%
Total errors	13	5.9%	33	8.1%	17	5%

Table 2.2.: Error analysis of the validation samples showing the absolute and relative number of errors and error types for each validation sample.

For all validation samples, the dominating error class is boundary errors. This is expected as the neural network is run with symmetric boundary conditions at the border of the structure. Fiber contact errors in validation sample 2 were mainly caused by two clusters of multiple thin fibers touching in the same place. However, I did not observe this configuration when validating real images. The validation dataset and the results are available for download [2].

2.5.2. Real Data

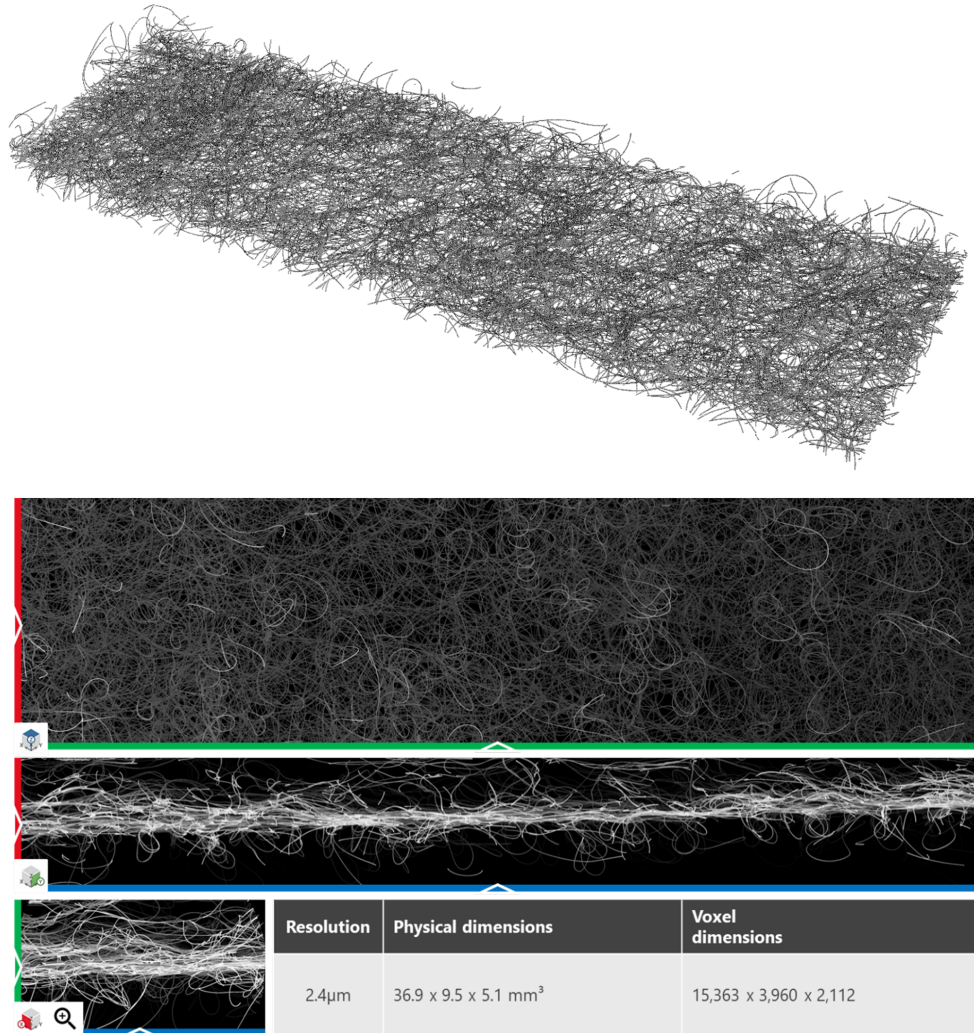


Figure 2.10.: 3D and 2D view of Sample C.

I demonstrate the method presented here on two material samples. The materials under consideration are bulky nonwoven fabrics. According to WO2020/103964 A1 [51], these materials can be used in the hygiene industry as components of absorbent hygiene products (e.g. baby diapers, incontinence products, female hygiene products, changing pads, etc.). The two samples are composed of synthetic round fibers. The fiber diameter varies slightly within each sample, and the samples differ in fiber density and distribution of fibers. Bruker acquired multiple scans per sample on a SkyScan 1272 micro-CT. These individual scans were stitched together along the x-Axis to create the full-sized scan. The first sample, Sample C (Figure 2.10), was scanned at a resolution of 2.4 μ m and has dimensions of 15,363 x 3,640 x 2,112 for a total of 118,958,443,614 vox-

els. Sample C is available for general access [58]. The dataset contains the original micro-CT, the segmented binary raw image, the labeled raw image where every fiber has its label, and the analytic description of the centerlines of the fibers. The second sample, Sample B (Figure 2.11), was scanned at a resolution of $2.7\mu\text{m}$ and has dimensions of $15,619 \times 4,032 \times 1,796$ for a total of $113,104,551,168$ Voxels.

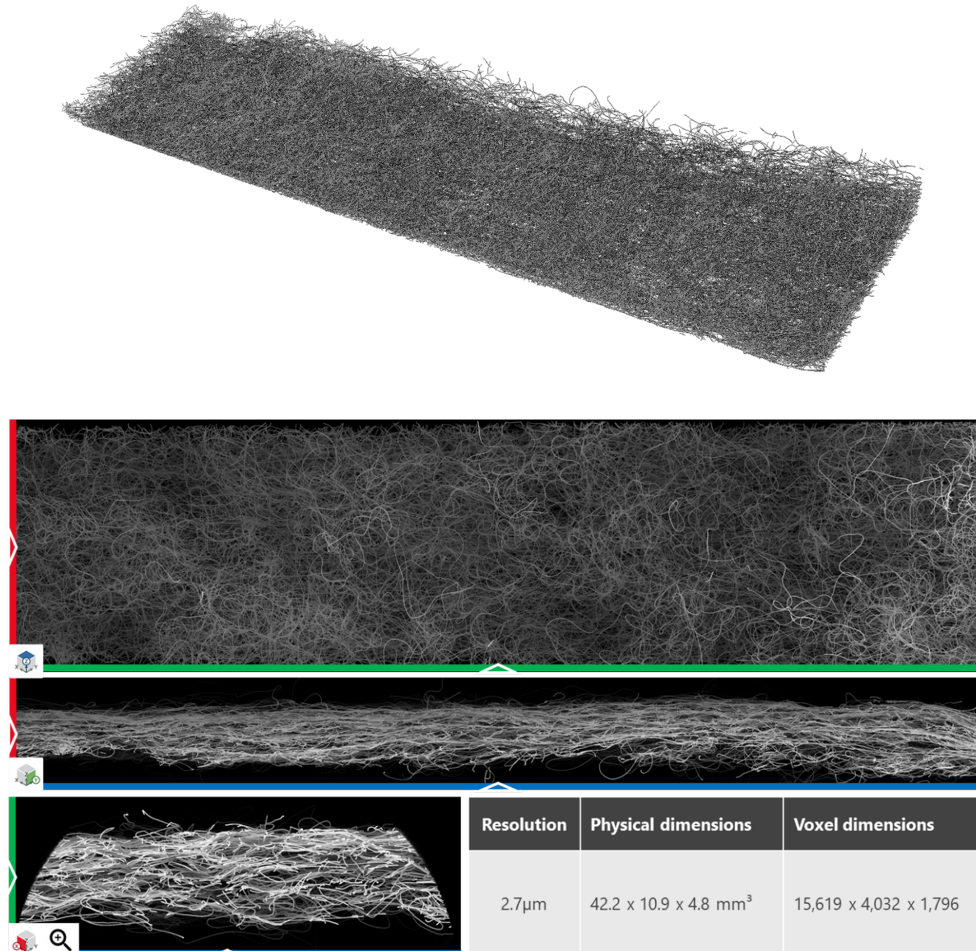


Figure 2.11.: 3D and 2D view of Sample B.

The datasets' sizes required the algorithm to be extremely fast and memory efficient. Before taking the scans, the samples were aligned to have the principal fiber direction in the x-axis so that the scans contained very long fiber segments. I applied the method presented to both samples to characterize differences in the fiber geometry of the samples. The results of this analysis were used in the patent WO2020/103964 A1 [51] to demonstrate differences between two manufacturing processes. Figure 2.1 depicts the clear advantage of using the neural network-based centerline detection compared to

morphological skeletonization. The centerlines were calculated for two fibers in contact over a longer distance. The reconnection step can easily connect the gaps in the AI-derived centerline. In contrast, the morphological skeleton collapses to a single centerline in the area where the fibers are parallel.

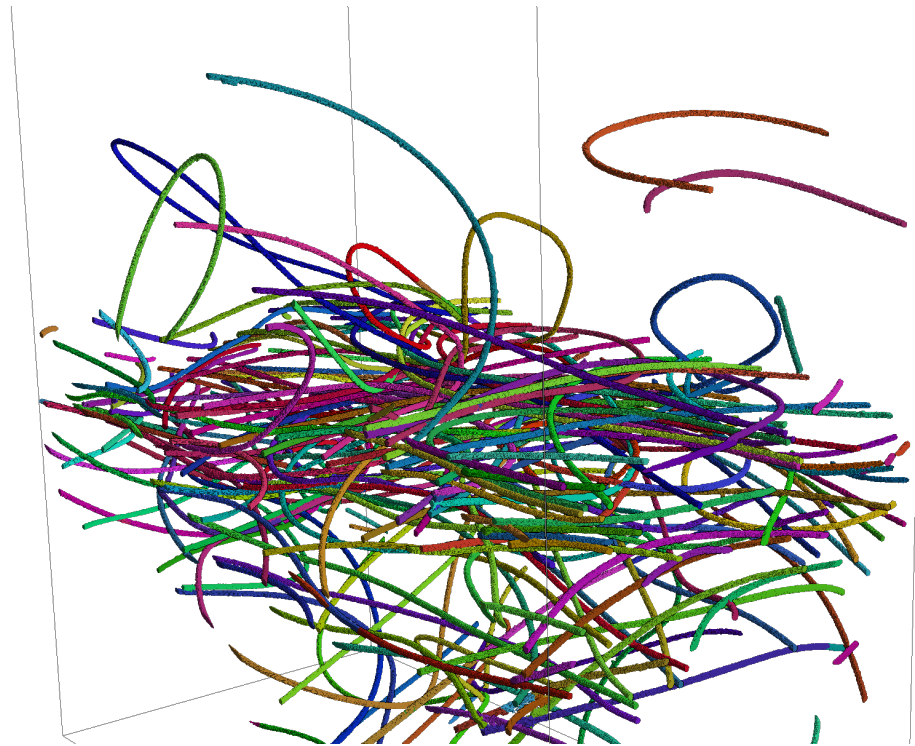


Figure 2.12.: *Sub-volume of Sample C (2000 by 1000 by 2112 Voxels) with labeled fibers.*

Figure 2.12 shows a 2000x1000x2112 voxel sub-volume of Sample C where the fibers have been labeled with unique IDs. The IDs are visualized in distinct colors, showing the successful identification of individual fibers in the complex fiber network. Figure 2.13 displays the complete labeled fiber network of Sample C. Half of the domain shows the labeled voxels (colored), the other half shows the segmented structure (gray). Figure 2.14 shows the same result for the denser fiber network of Sample B. The training was done only once, and Sample B was analyzed using the neural network trained for Sample C. The models used in the training data were generic enough that the change in resolution between Sample C and Sample B did not negatively affect the results.

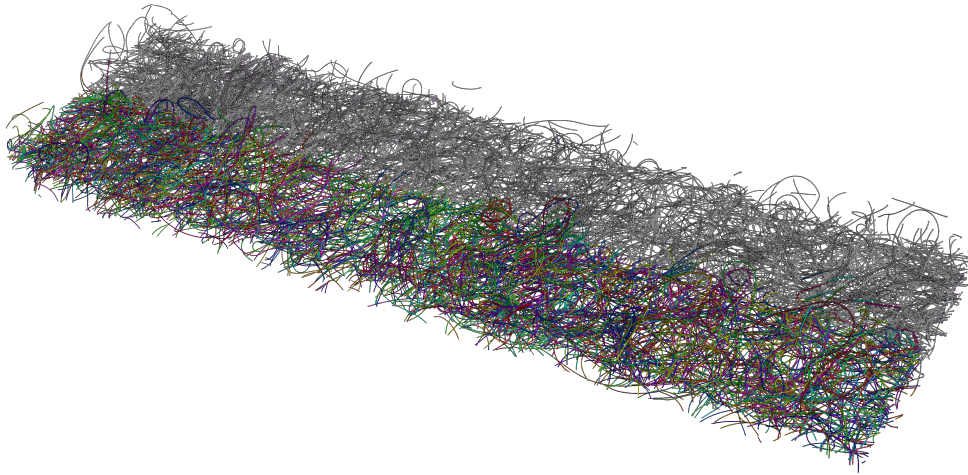


Figure 2.13.: *Split view of the Segmented Sample C and the labeled fibers colored in different colors.*

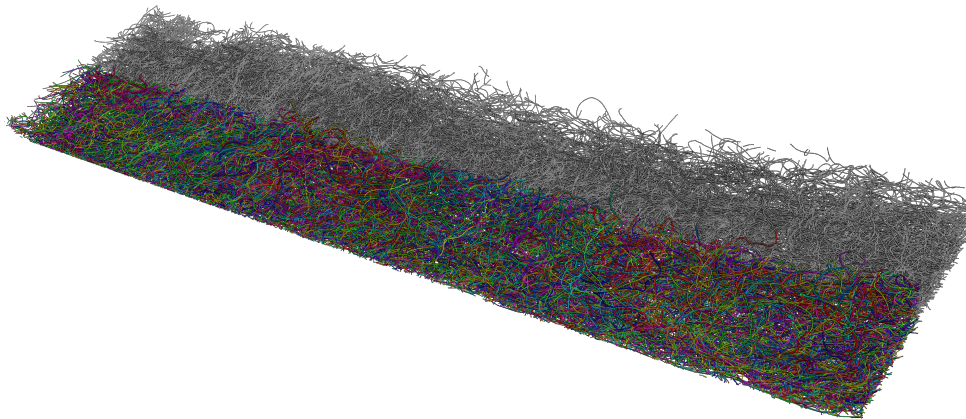


Figure 2.14.: *Split view of the Segmented Sample B and the labeled fibers colored in their individual colors.*

For Sample C, the total number of fibers detected was 3352. For Sample B, 11327 fibers were detected. Two geometric properties of the fibers of interest in the patent WO2020/103964 A1 [51] are the fiber curvature distribution and the fiber curl-index distribution. Particularly, the analysis of the fiber curl-index made it necessary to use a large field of view for the scan.

As visible in Figure 2.15, the trajectory of a single fiber within a nonwoven material can become complex and using only a small field of view would not reveal this. For the analyzed samples, the mean fiber curl-index of Sample C

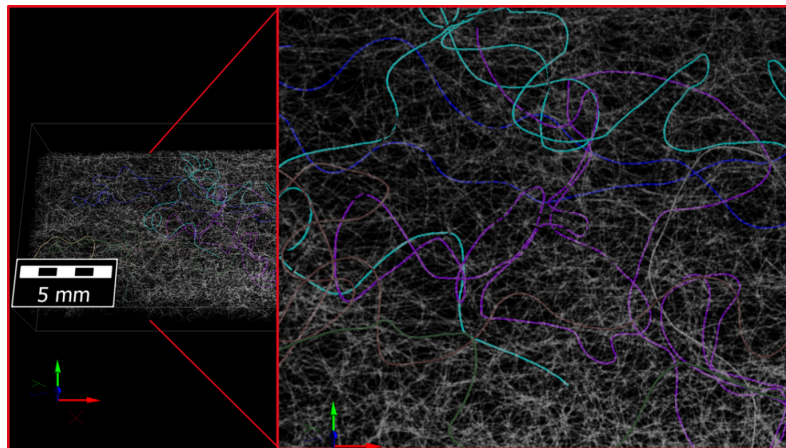


Figure 2.15.: Some fibers of Sample B colored. The remaining fibers are rendered transparent.

proved to be higher than the curl-index of Sample B. For sample C the mean curl-index is 5.8; for sample B the mean curl-index is 2.9. This observation aligns well with the expectation of the manufacturer and the visual observation that Sample B generally looks more oriented in the machine direction (the x-axis). The mean curvature of Sample B was measured to be lower too, matching the curl-index results (Figure 2.16). For Sample C, the orientation was analyzed in multiple layers (Figure 2.17), revealing a stronger orientation in the machine direction towards the center of the material. In contrast, the top and bottom layers contain many fibers deviating in the Z-direction and later looping back into the main material sheet (Figure 2.17).

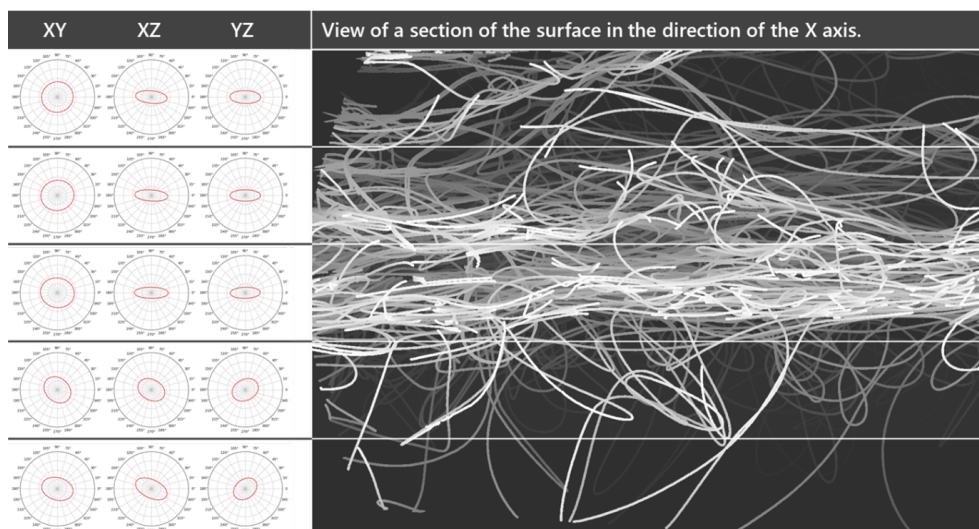


Figure 2.17.: Orientation analysis of Sample C. The columns on the left show the orientation tensor visualized in the three main planes.

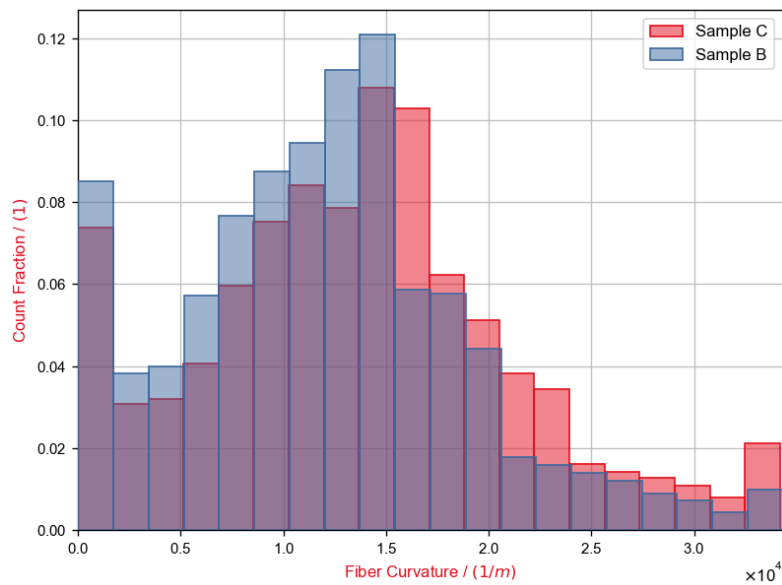


Figure 2.16.: Comparison of the curvature distribution of sample B and C.

2.5.3. Conclusion

I demonstrate that the approach presented in this work can identify individual fibers in CT scans of nonwovens. The validation shows that the method is robust for samples that do not deviate too far from the parameters of the training data. I conclude that it is feasible to train neural networks on artificially generated models of nonwovens and apply them to the analysis of CT scans of real materials. This method avoids the time-consuming and error-prone process of manually labeling data. It can be easily adapted to other fibrous materials by modifying the generator parameters. One such example could be fiber-reinforced composite materials.

2.6. Core Reference

- A. Griebner, R. Westerteiger, E. Glatt, H. Hagen, and A. Wiegmann, “Identification and analysis of fibers in ultra-large micro-ct scans of nonwoven textiles using deep learning,” *The Journal of The Textile Institute*, vol. 114, no. 11, pp. 1647–1657, 2023. DOI: 10.1080/00405000.2022.2145429

3. Segmentation of binder and fibers in gas diffusion layers

Contents

3.1. Abstract	25
3.2. Introduction	26
3.3. Related Work	27
3.4. Method	29
3.4.1. Training Data	29
3.4.2. Neural Network	32
3.5. Results	34
3.5.1. Synthetic Data	34
3.5.2. Real Data	37
3.5.3. Conclusion	40
3.6. Core Reference	41

3.1. Abstract

Gas diffusion layers (GDLs) are vital for the performance of proton-exchange membrane fuel cells (PEMFCs). In many cases, they are made of Carbon-Carbon Composite Paper (CCCP), which consists of carbon fibers and a carbonized binder material. The distribution of the fibers and binder in the GDL strongly influences the performance of a PEMFC. Synchrotron scans are a great way to obtain information about the microstructural composition of carbon paper GDLs (Figure 3.1), but one major obstacle exists. Binder and fibers tend to have the same attenuation and, consequently, the same gray values in the scans. To overcome this, a machine learning-based method is introduced that segments fibers and binder from the local morphology of a CCCP. The training data is generated using FiberGeo, a module in the GeoDict software for fibrous microstructure generation. FiberGeo creates fibers based on stochastic geometry and adds binder using morphological opening and closing operations. I applied the machine learning-based method to four Scans of samples of Toray Carbon Paper with varying amounts of binder in them. The result is the classification of individual voxels as fiber or binder material that can be used, for example, in performance simulations of property simulations in PEMFCs [59][60][61][62]. Here, the focus is on the differences in

the spatial distribution of the binder both in the through-plane and in-plane directions.

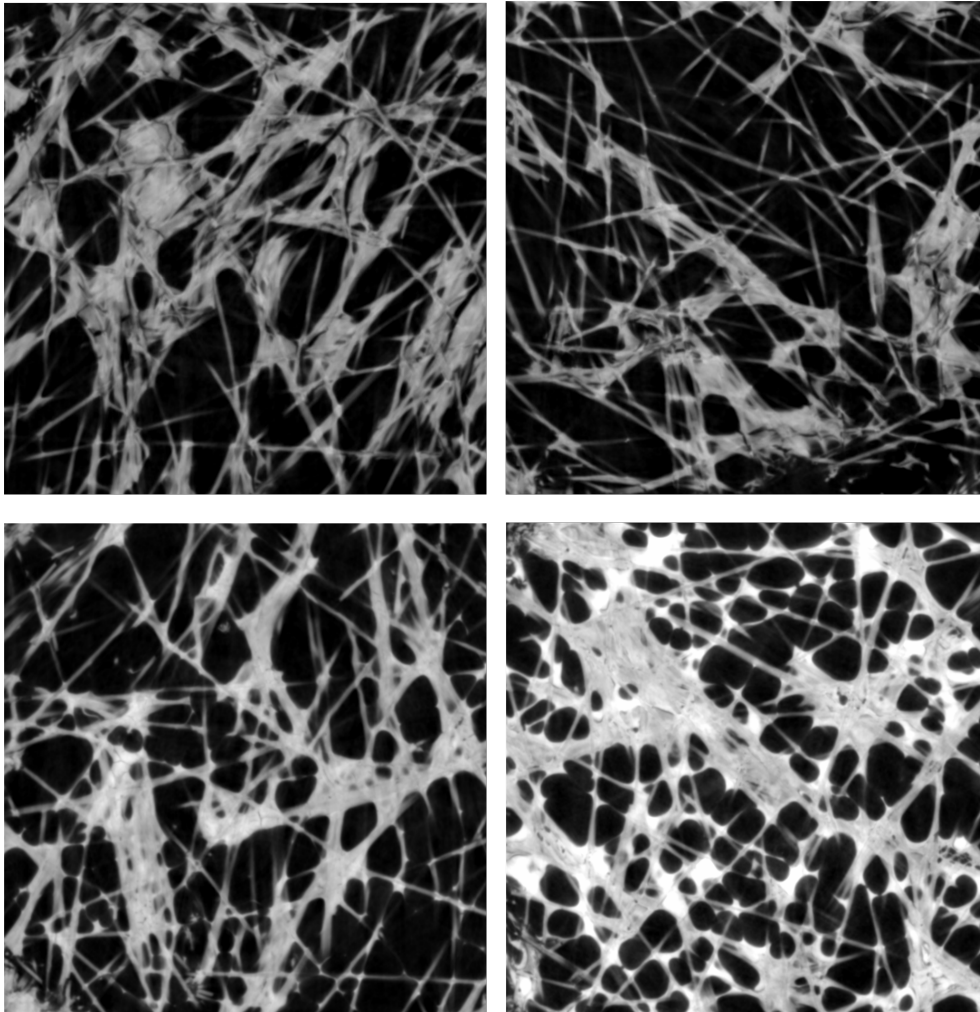


Figure 3.1.: : Four 2D slices of Toray Carbon Paper TGP-H-030 with different amounts of wet proofing (top left: GDL1 5% wet proofing, top right: GDL2 10% wet proofing, bottom left: GDL3 30% wet proofing, bottom right: GDL4 50% wet proofing).

3.2. Introduction

Gas diffusion layers (GDLs) are a vital part of fuel cells. The GDL is located between the catalyst layer (CL) and the flow field plate on the anode and on the cathode side of a fuel cell. The GDL distributes the reactant gases towards the CL while controlling the amount of water in the CL and mechanically supporting it. Besides that, good thermal conductivity is necessary for heat management in the fuel cell [63]. A high electrical conductivity is required to transport the electrons from the CL to the flow field [64]. All

these requirements make the GDL an essential part of the operation of Proton Exchange Membrane Fuel Cells (PEMFCs), Direct Methanol Fuel Cells, and Phosphoric Acid Fuel Cells.

To maximize the performance of a fuel cell, it is vital to design the GDL accordingly. This has been subject to much research in the past, which is presented extensively in the review paper by Cindrella et al. [65]. Designing the GDL requires a good understanding of the functionality of its microstructure. I focus on analyzing carbon paper GDLs, as this material is relatively cheap and widely used. Another typical GDL material is carbon cloth [66], which is not further investigated here. Design parameters to optimize in a carbon paper are the amount of binder and the distribution of hydrophobic and hydrophilic surfaces throughout the GDL. The binder keeps the fibers connected, providing mechanical stability and conducting pathways through the material. Negatively, more binder reduces the diameters of the flow channels through the material and hence the diffusion of the reactant gases. A polytetrafluoroethylene (PTFE) coating is usually added to the material in addition to the binder. The PTFE makes the GDL more hydrophobic and thus helps manage the amount of water in the GDL and the CL [64].

To simulate the influences of the amount of PTFE and binder in carbon paper, it is necessary to apply the correct physical properties to the two materials. The segmentation into three phases (pores, fibers, binder+PTFE, Figure 3.2) is notoriously difficult because in a micro-computed tomography (micro-CT) scan or synchrotron scan, the carbon fibers and the carbonized binder and PTFE often have the same attenuation [67]. I approach this problem by using an artificial neural network trained on generated data to create the 3-phase segmentation. A differentiation of binder and PTFE was not attempted, so when referring to binder in this work, the combination of binder and PTFE is meant.

3.3. Related Work

Many different approaches to segmenting materials phases in images using machine learning (semantic segmentation) exist and have been deployed successfully. One example is the trainable WEKA segmentation [24]. This approach uses manual labeling on 2D images to obtain training data. However, manual labeling of images is very time-consuming. It is also error-prone, with results depending heavily on the expertise and experience of the user. I tested segmenting the binder and fibers directly from the grey value images using a similar approach and did not achieve good results, as labeling binder fibers in the grey value images, even manually, is a difficult task. Another notable approach using deep learning for segmenting minerals in rocks is by Phan et al. [25], who train an improved U-Net architecture to segment pores and minerals on micro-CT scans of rock samples. They start from high-quality scans of multiple rock samples, segment each using existing segmentation methods, and enhance this training dataset with artificially added artifacts. A similar process on a single rock type is presented by Karimpouli et al. Al. [26]. The

approach presented in this work differs from these methods by generating the training data completely from models, using 3D fiber and binder modeling tools available in the GeoDict software [27]. Generating completely artificial models eliminates the necessity of scanning many samples for training. The workflow to segment fibers and binder starts on scans segmented into solid and pore space, as the modeling tools used can only create segmented images. In the future, it is desirable to add synchrotron and micro-CT artifacts to such training data and develop a workflow that starts with the gray value images. This capability is currently under development at Math2Market ¹ and is also available from other researchers [68]. Deep learning-based approaches to segment GDLs have also been used by Tang et al. [28] and Mahdaviara et al. [29]. In both works, a segmentation of binder and fiber similar to this work is achieved. In contrast to this work, they start from scans in which there is a contrast in grey values and fibers. This contrast allows the creation of training data for the deep-learning part by semi-automatic tools. There have also been attempts to segment binder and fiber using classical approaches. One such approach is presented by Chen et al. [30], who use a multi-threshold non-local means joint distribution method to find the distribution of fibers and binder. In contrast to the approach presented in this work, they require a difference in grey values between fibers and binder for the approach to work. The modeling approach used for the binder in this work is similar to Simaafrookhteh et al. [31], who create the binder phase in 3D scans of GDLs using morphological operations. They also investigate the effect of different amounts of binder on carbon paper's permeability, diffusivity, and thermal conductivity. The same approach of adding binder by morphological operations to investigate the effects on performance has been used for batteries by Hein et al. [32] and Trembacki et al. [33]. Similarly, Wang et al. [34] investigate the impact of hydrophobicity on the water transport velocity of Toray GDLs. Their approach alters the GDLs by adding hydrophobic decorations on top and bottom, changing morphology and fiber diameters, and increasing the breakthrough pressure. More work on the impact of the amount of binder on the performance of a GDL has been done by Flückiger et al. [35]. They experimentally studied different binder amounts and PTFE treatments on GDLs and concluded that binder amounts over 50% negatively impact effective diffusivity. Yiotis et al. [36] study the influence of binder on the performance of a GDL by generating models using the same approach to create the fiber network as used in this work. Investigating the performance of GDLs and other parts of fuel cells by simulation has been an approach adopted in many works, for example Zamel et al. [37], Hrandi et al. [38] or Simaafrookhteh et al. [31]. For these works, obtaining a separation of the fiber and binder phases in micro-CT scans of GDLs is beneficial to account for their different physical properties in simulations. The approach presented in this work models GDLs as training data for a neural network in a two-step process. First, a fibrous structure is created using a Poisson line process. Then, the binder distribution in the fiber structure is simulated using morphological operations. The basic idea of the first

¹<https://www.math2market.com>

step is described by Schladitz et. al. [39]. Straight, infinitely long, potentially overlapping fibers are generated from a Poisson line process according to an anisotropic direction distribution and a given fiber diameter distribution. This approach gets statistically correct fiber distributions in finite-sized domains. The approach is extended by moving and bending the fibers after the initial creation to allow the fibers to overlap only a defined amount.

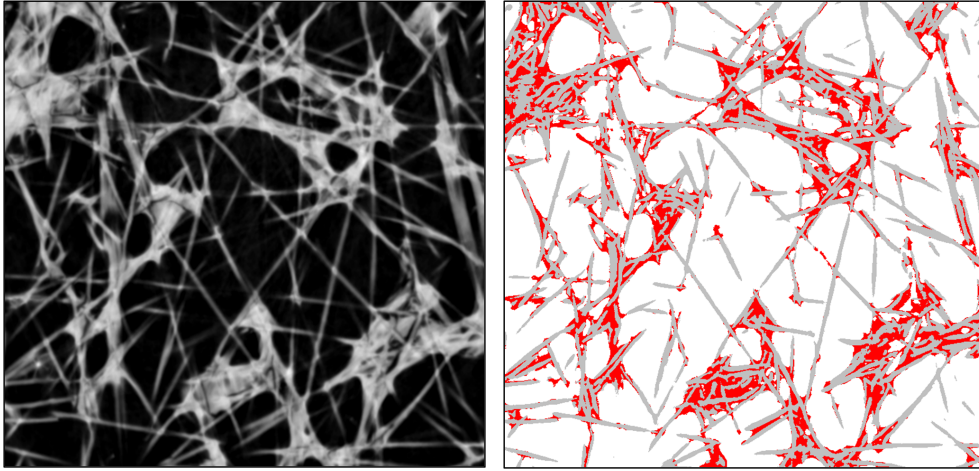


Figure 3.2.: Grey value image and segmented result of the method from this work showing fibers in grey, binder in red and pores in white.

3.4. Method

Taking micro-CT or synchrotron images of carbon paper as used in GDLs results in images where binder and fiber have the same attenuation. This can be observed in Figure 3.1, which shows slices of a synchrotron scan of such a GDL. It is only possible to segment pores and solids (fibers and binder) into a binary image from these scans by attenuation. Yet the fibers and binder are easily differentiable for the human eye. The strong distinction between the local shapes of round fibers and the typical concave surfaces of binder can explain this. This strong shape distinction motivates the idea to use a machine-learning-based approach to segment binder from fibers in segmented 3D scans of GDLs.

3.4.1. Training Data

The acquisition of sufficient and good-quality training data is crucial to the success of every machine learning-based method. Specifically, neural networks require large amounts of labeled training data. In my case, this would be images where fibers and binder are segmented in different colors. Obtaining such images is not easy. It would require either adding a marker to the binder before production to make it visible in the scan or manually labeling the binder and fibers in different colors in 3D digital scan data. The first approach is

costly as it would require custom sample production. The second approach is often applied for 2D training data generation, such as categorizing a few objects in photographs. Labeling each voxel in multiple 3D datasets is costly, as it would take a lot of hours to do the segmentation manually. I decided to use material model generation to obtain training data.

Math2Market’s GeoDict software provides multiple modules to create models of a wide range of material types. For the case presented here, I used FiberGeo [69] to generate the base fiber structure and add binder afterward. All material information is preserved in the generated models, and fibers and binder are generated with different labels. Developing a so-called stochastic digital twin of a real material is possible with these tools. A digital twin is a digital representation of a real-world object, such as a CAD model for car crash simulations.

In contrast to the exact CAD model, a stochastic digital twin is a material model with the same average geometric properties (e.g., pore size distribution, fiber diameter distribution, binder volume percentage, etc.) and physical properties (e.g., permeability). A statistical digital twin of a material is as similar to a digitalization of an actual sample of that material as another digitalization of another real sample of the same material (e.g., taken from another location) would be. This is feasible for material models as, typically, the characteristics of materials are best described by distributions of properties such as fiber diameters or pore sizes. By entering these characteristic parameters into the model generators, it is possible to create many different realizations of such a stochastic digital twin and its siblings, i.e., models with similar characteristics but that are not statistically identical. This allows us to create arbitrary amounts of 3D training data that can cover various ranges of geometry parameters quickly [49]. The only manual work that remains to be done is setting up the input parameters for the generator in a way that the created training data covers the parameters of the material that should be labeled.

Model generation for training data

The process must create training structures that capture the characteristic features of the material to analyze. The focus must be matching the typical local look of a segmented micro-CT scan of such a material. By varying the amount of binder content and the fiber diameters, I ensure that the network will not overfit the provided training data and can be generalized for use in differently manufactured GDLs. I train the neural network with models of carbon paper GDLs that are generated using a two-step process. In the first step, straight fibers are generated using the fiber generator. I set up these fibers to be isotropically oriented in the X-Y Plane, like the micro-CT scans of most real GDL materials. As described by Schladitz et al. [39], the core method uses a Poisson line process to generate appropriately distributed fibers in the model domain. The density function gives the fiber directions in the

generation process:

$$p(\theta, \varphi) = \frac{1}{4\pi} \cdot \frac{\beta \cdot \sin(\theta)}{(1 + (\beta^2 - 1) \cdot \cos^2(\theta))^{\frac{3}{2}}} \quad (3.1)$$

β is the so-called anisotropy factor that allows control of how parallel the fibers should be to the Z-plane. Higher values of beta yield more planar distributions.

The approach is extended by an overlap removal step that shifts the fibers randomly until the allowed remaining overlap is reached. The fibers were allowed to overlap by one micron to account for deformations and CT artifacts that happen at the contact points of fibers in segmented scans of the actual material. These fiber-fiber contact points in 2D never look like two touching circles but more like hourglasses. The generation method closely reproduces this morphology (Figure 3.3).

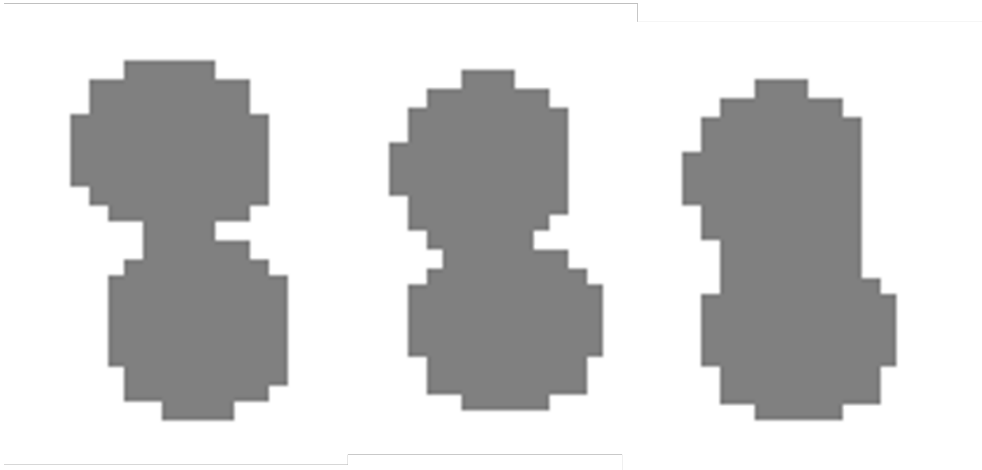


Figure 3.3.: Example of generated fibers at 10 voxels fiber diameter. Left: no overlap, center one voxel overlap, right: 1 voxel overlap and small amounts of binder added to smooth out the contact.

In the second step, I add binder to the fiber structure. The binder is added using dilation followed by erosion [59], which is called morphological closure in the stochastic geometry literature. The binder is usually distributed anisotropically in the sense that it spreads out further in the fiber planes and less in the through-plane direction. The binder generator accounts for this by first stretching the structure, then adding the binder isotropically, and then compressing the structure again. I obtained the ground truth needed to train the neural network by adding the binder to the structure with a different label from the fibers. The method presented for generating training data closely matches the actual samples, as shown in Figure 3.4. There might be inhomogeneities in the binder/fiber distribution or fiber shapes that were not captured in the training data, leading to errors when applying the model to actual samples. Differences in the projected 2D in-plane distribution of solid material can be observed in the training data compared to the actual samples. While the generated samples have a homogeneous distribution of fibers and binder, the

actual samples have a more spread-out distribution. The standard deviation of the density distribution in the through-plane direction is 0.074 for the real samples compared to 0.056 for the generated training datasets.

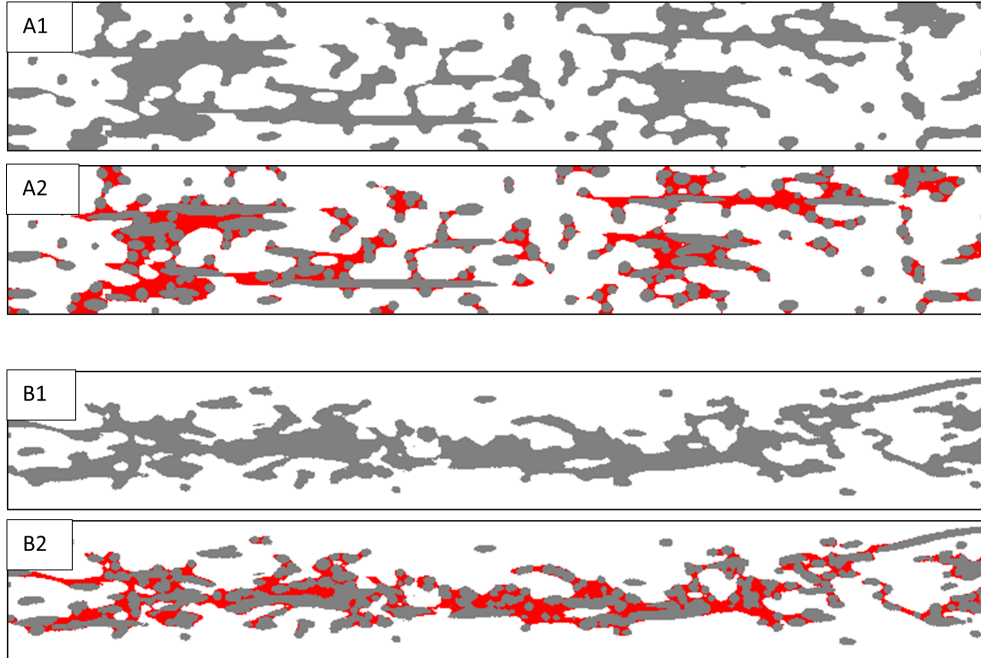


Figure 3.4.: Example of in-plane slices of training data and real samples. A1: input image for supervised learning A2: output image for supervised learning B1: GDL1 segmented into pore and solid space B2: GDL1 segmentation of binder fibers and pore space using the method from this work.

The amount of binder and fibers in the training data models varies to account for variations within one sample and over a range of samples, thereby allowing the network to generalize better. The neural network was trained on 100 artificial carbon paper models generated with GeoDict. To account for variances between samples, the solid volume percentages of fibers, the fiber diameters, and the amount of binder were varied between the training models in a range larger than in the actual samples. All training models were 800 by 800 by 120 voxels (Figure 3.5).

3.4.2. Neural Network

Model generation for training data

For the Deep Learning part of the algorithm, TensorFlow [52] is used. As a network architecture, I choose a variation of the widely used U-Net [53]. Originally only used in 2D, I extended the network to a 3D architecture like [70]. Volumetric data is fed into the network, returning a smaller but still volumetric sub-window. I train the neural network using supervised learning. This means that inputs and corresponding outputs are passed to the train-

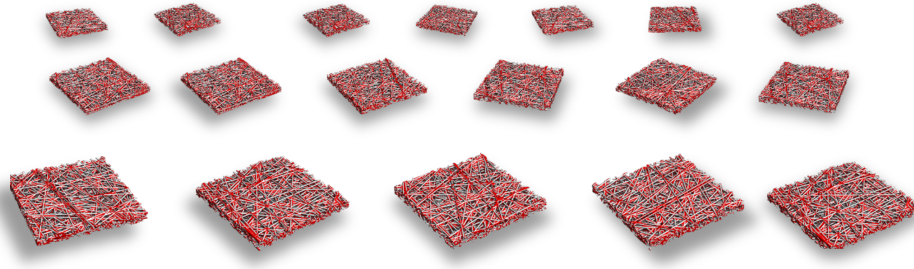


Figure 3.5.: Visualization of a subset of the 100 artificially generated training samples. All training structures are generated similarly, but key properties like the number of fibers and the amount of binder vary from structure to structure.

ing algorithm, and the network learns how to transform the input into the corresponding output using a gradient descent optimization. During training, the whole structure is not passed into the network at once to avoid memory limitations. Instead, it is subdivided into sub-windows of size 91 by 91 by 52 voxels so that the output windows cover the whole input structure.

Training on sub-samples

Using a 3D network architecture instead of a 2D slice-based approach comes at the cost of longer training times and a demand for more training data. The latter is irrelevant for this work, as the amount of training data that can be generated is practically unlimited. The time it takes to create the training data can be disregarded compared to the time it takes to train the network. The benefit of using the 3D U-Net lies in the quality of the results. To avoid being limited to fixed image sizes, I do not apply the neural network to the whole image all at once. Instead, a sliding input window is passed over the image. A smooth and flicker-free result is generated by considering a 3D context bigger than the network’s output size. To keep the size of the input window and the training times manageable, the depth of the U-Net was reduced to two, but the training framework was designed in a way that window sizes and U-Net depth can be adapted if required (similar to 2.4.4).

Transfer to real data

After training and validation on generated data, the network is applied to binarized real synchrotron scans. The pore space is kept, and the solid phase is again binarized into fibers and binder. The output of the whole process is thus a new image where the binder and fiber phases are separated, resulting in a three-phase image of pore space, fibers, and binder. This three-phase segmentation allows further insights into the characteristics of the binder in the material, such as the distribution in-plane and through the material’s

thickness or the homogeneity of the binder distribution. On top of this, more detailed simulations can be run, such as conductivity simulations that consider different conductivities in binders and fibers.

3.5. Results

3.5.1. Synthetic Data

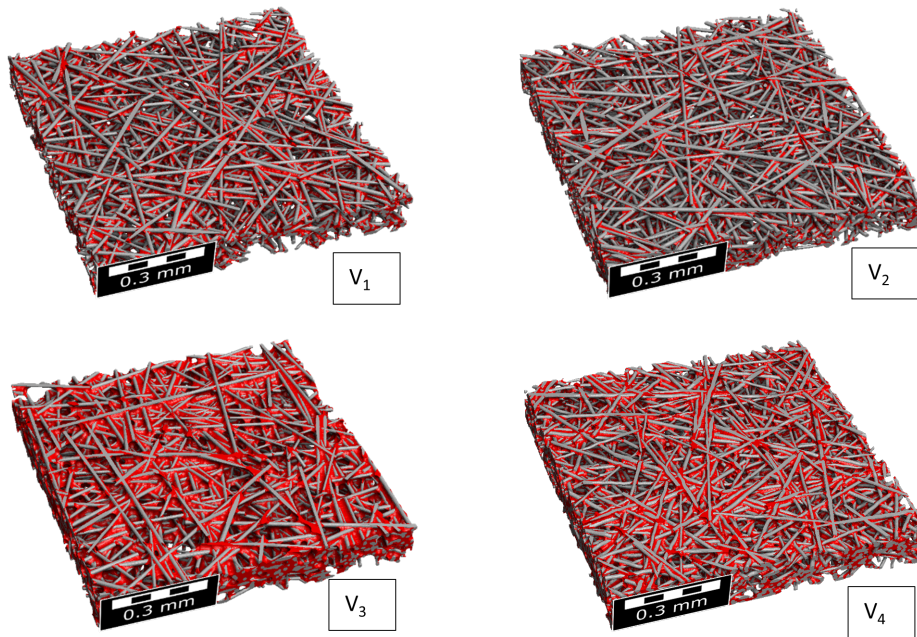


Figure 3.6.: Validation datasets: top less binder, bottom more binder; left fewer fibers, right more fibers.

To validate that the presented approach can label binder correctly, I use four validation data sets V_1 , V_2 , V_3 , and V_4 with dimensions 800 by 800 by 120 voxels as known ground truth. The samples were created with FiberGeo using parameters (Table 3.1), such as the parameters of the materials evaluated in the result section (Table 3.4). I then compared the results of applying the trained neural network to the ground truth to quantify the error that is to be expected from the method. The fibers in the validation data sets were generated at a voxel length of $1.3\mu\text{m}$ and with a small amount of overlap allowed. The samples vary in amounts of binder, amount of fibers, and total solid volume percentage to let the neural network handle such variations in the materials. Table 3.1 and Figure 3.6 show the complete overview of the varied parameters.

Ground Truth	V1	V2	V3	V4
Fibers / (%)	15.63	21.89	15.64	21.87
Binder / (%)	10.46	10.35	14.58	20.78
Solid Volume / (%)	26.09	32.23	30.23	42.64
Porosity / (%)	73.81	67.77	69.77	57.36

Table 3.1.: Solid Volume percentages of the four validation samples.

Identified	V1	V2	V3	V4
Fibers / (%)	15.55	22.03	15.41	21.65
Binder / (%)	10.54	10.20	14.82	21.00
Solid Volume / (%)	26.09	32.23	30.23	42.64
Porosity / (%)	73.81	67.77	69.77	57.36
Binder as Fiber Error / (%)	3.11	3.65	3.87	6.21
Fiber Binder Error / (%)	3.42	3.20	4.65	6.73
Solids Error / (%)	6.53	6.85	8.52	12.93
F_1 Score	0.92	0.89	0.91	0.87

Table 3.2.: Error analysis on the validation structures.

Analyzing the quality of the results on the validation structures yielded absolute relative errors between 6.5% and 12.9%. A commonly used metric for the performance of a classification task is the $F1$ score:

$$F_1 = \frac{2 \cdot tp}{2 \cdot tp + fp + fn} \quad (3.2)$$

Where tp is true positives (binder as binder), fp is false positives (fiber as binder) and fn is false negatives (binder as fiber). I achieved $F1$ scores between 0.87 and 0.92 (Table 3.2). The error increased with the increased total solid volume percentage of the samples. A more detailed analysis of the results showed that the errors occurred mainly in big binder accumulations (Figure 3.7). This effect could be explained by the limited perceptive field of nodes in the lower layers of the U-Net, which does not consider the surrounding area of the accumulations, and more homogeneous binder distributions in the training data. Another primary error source is voxels at the boundary of fibers that are wrongly classified as binder. This error class has only a minor influence on the morphology of the result. When transferring from the artificial validation dataset to a real one, I expect the observed error to be a lower bound for the actual error. The real dataset might contain configurations of fibers and binder that I did not capture in the training dataset. To assess the impact of this error, I simulated the electrical conductivity of V_1 based on the ground truth image and the results of the binder identification. For the simulation, I assumed the carbon fiber to be 100 times more conductive than the binder material. I observed a decrease in in-plane conductivity by 3.4% and an increase in through-plane conductivity by 5.2% (Table 3.3).

Conductivity	V1 Ground Truth	V1 Result	Error / (%)
In-plane / (S/m)	4201.3	4059.9	-3.4
Through-plane / (S/m)	304.0	319.8	5.2

Table 3.3.: Error of conductivity due to errors in detection of fibers and binder.

Ground Truth	GDL1
Fibers / (%)	16.32
Binder / (%)	5.58
Solid Volume / (%)	21.90
Porosity / (%)	78.10

Table 3.4.: Solid Volume percentages of the manually labeled GDL1.

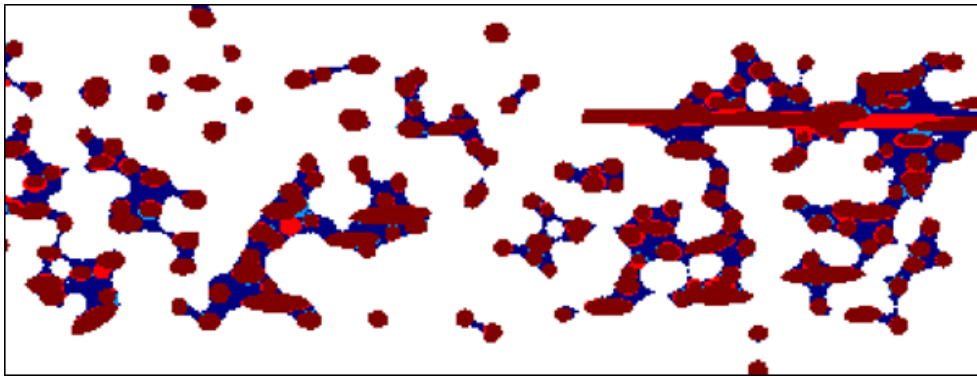


Figure 3.7.: Four color image showing correctly labeled fibers in dark red and correctly labeled binder in dark blue. Fiber material that has been labeled as binder is shown in bright red, and binder that has been labeled as fiber is shown in light blue. A typical error is visible in the top right: A fiber is not traced completely through a bigger binder accumulation.

On top of the validation on the artificial dataset, I performed a validation on one of the real datasets (GDL1, more details in the results section) by manually labeling a small cutout of the dataset. The volume fractions of the cutout can be seen in Table 3.5. To obtain the labeling, individual fibers in areas with little binder were searched and then traced through the bigger binder accumulations. For this validation, I expected the error to be higher than for the artificial dataset, but still within 15%. The manually labeled cutout had the following properties:

I applied the same metrics as before to inspect the quality of the result.

The result shows a slightly worse performance for this validation compared to the artificial dataset. Nevertheless, the error is still below 10% and therefore in an acceptable range. The errors observed were similar to the ones observed on the validation dataset, showing no indication of a systematic error in the method presented here (Figure 3.8, Figure 3.9).

Identified	GDL1
Fibers / (%)	15.32
Binder / (%)	6.58
Solid Volume / (%)	21.90
Porosity / (%)	78.10
Binder as Fiber Error / (%)	2.63
Fiber Binder Error / (%)	7.17
Solids Error / (%)	9.80
F1 Score	0.82

Table 3.5.: Error analysis on manually labeled GDL1.

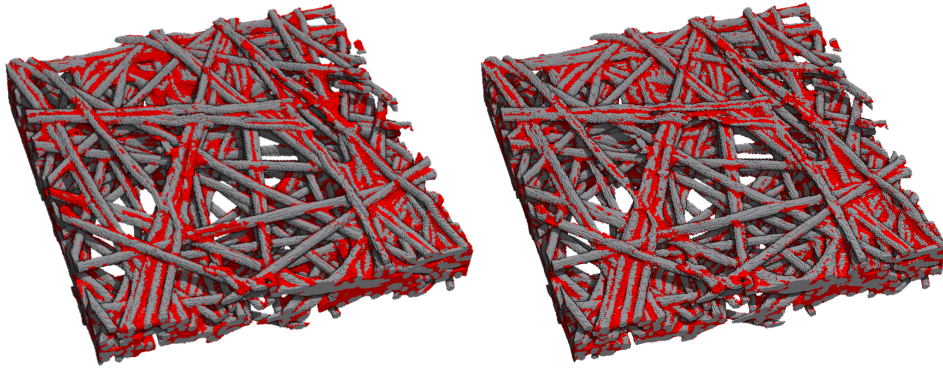


Figure 3.8.: Left: Manually labeled crop of GDL1. Right: Output from the method presented here.

3.5.2. Real Data

I demonstrate the method on four real synchrotron scans of Toray Carbon Paper TGP-H-030, a material commonly used as GDLs in PEMFCs, in addition to the validation dataset. The four samples had varying amounts of binder and PTFE treatment. Figure 3.1 shows in-plane slices of the material scans. The fibers in the material are round carbon fibers, and the binder is a carbonized polymer with a coating made from PTFE to influence wettability. As seen in Figure 3.1, attenuation in the scan is the same for binder and fibers, making segmenting by thresholding impossible. To simulate the physical properties of the GDL correctly, it is desirable to segment binder and fibers, especially since their conductivity is very different. Each sample is roughly 800 x 800 x 80 voxels for a total of 51,200,000 voxels. I segmented the scans into pore space and solids using OTSU thresholding. The image did contain little to no noise, so no additional image filtering was required. The other preprocessing steps required were masking out the sample holder, straightening the slightly bent samples, and finally aligning them with the XY plane. Afterward, I applied

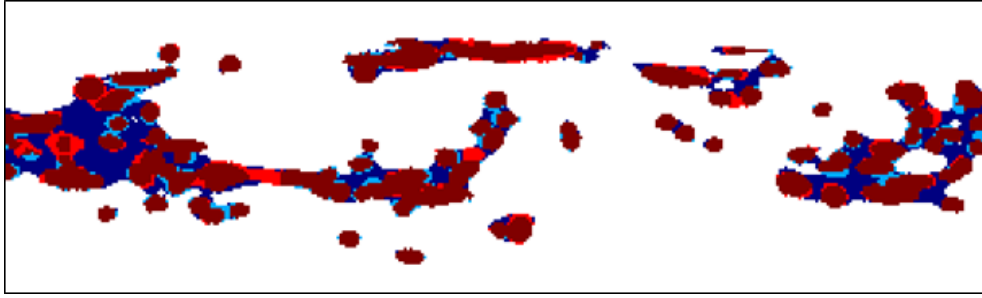


Figure 3.9.: Four color image showing correctly labeled fibers in dark red and correctly labeled binder in dark blue. Fiber material that has been labeled as binder is shown in bright red, and binder that has been labeled as fiber is shown in light blue. GDL1 with manual labels was used as the ground truth here.

the method presented here to all samples to characterize differences in the geometry of the samples. The distributions of the binder in the samples were mainly of interest. For these samples, the ground truth is unknown, so no direct quantification of the quality of the result is possible. We, therefore, relied on visual inspection and plausibility checks of fiber and binder distribution. The visual inspection of 3D images and 2D slices yields convincing results.

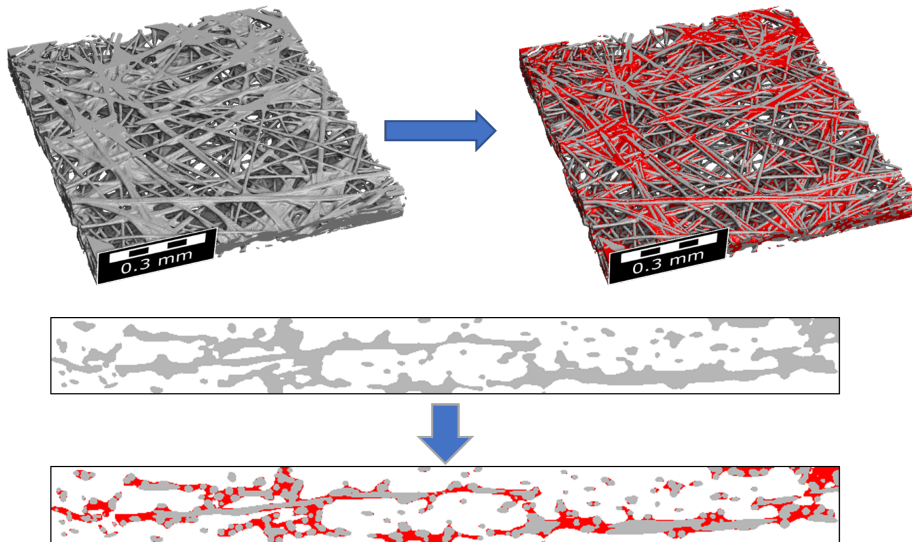


Figure 3.10.: GDL2 after binarization and after applying the method from this work to segment fibers (grey) and binder (red).

I compared the amount of binder and fibers detected in the samples (Figure 3.11). I expected the fiber amount to be similar for all the samples, as they are manufactured from the same base fiber network. The deviation in

Identified	GDL1	GDL2	GDL3	GDL4
Fibers / (%)	21.5	19.7	18.2	21.1
Binder / (%)	7.0	6.2	9.7	13.0
Solid Volume / (%)	28.5	25.9	27.9	34.1
Porosity / (%)	71.5	74.1	72.1	65.9

Table 3.6.: Voxel counts and solid volume percentages of the four synchrotron scans of gas diffusion layers.

fiber amounts for samples 2 and 3 can be considered within the margin of error already observed for the validation dataset.

Figure 3.11 shows the binder distribution in the samples through (z) direction. The distribution plots the middle slices of the material. This distribution pattern was expected, as the binder has the most fibers to attach to in these layers and can easily be caught in pockets of fibers. The distributions show the highest amount of fiber close to but not in the same slices as the highest amount of binder, supporting this observation.

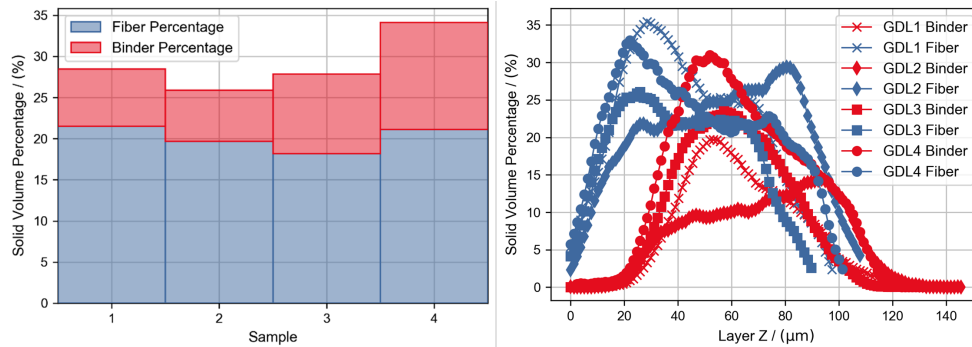


Figure 3.11.: Comparison of the amount of fiber and binder material detected in the four samples. Left: Total binder (red) and fiber (blue) percentages. Right: Distribution of fiber (blue) and binder (red) fractions in each z slice.

Finally, I compared the investigated density projections of the four materials. For each material, the projected density of all solids, the binder, and the fibers in the z-plane is plotted (Figure 3.10). These projections show a nice separation of the 2 phases. While the fibers are mostly homogeneously distributed with some more and some less dense areas, the binder phase is heavily inhomogeneous. As expected, the areas with high binder density correlate with areas with higher fiber density due to more binder sticking to the fibers in small pores.

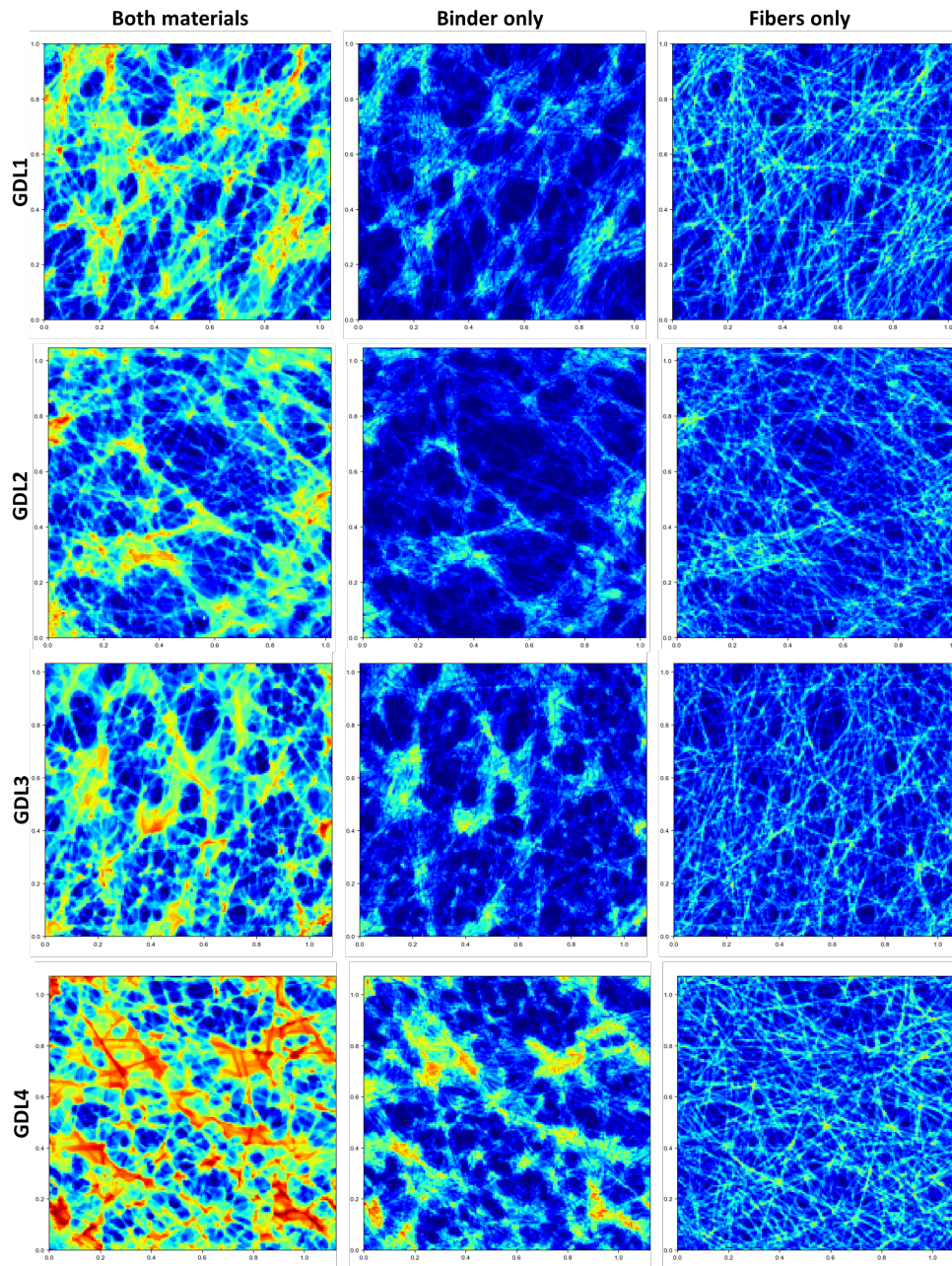


Figure 3.12.: 2D density projections in the through-plane direction of all samples showing the overall material, only the fiber material, and only the binder material. Color scales have been set to 0 (dark blue) to 1 (red) for all plots.

3.5.3. Conclusion

I demonstrated that the approach presented here can label binder in tomographic scans of GDLs. The validation showed that the method is robust for samples with solid volume percentage below 35% that do not deviate too far

from the parameters of the training data. Better results might be possible with more refined training data for a higher solid volume percentage. The use on actual scan data showed that the network performed well even though it was only trained on computer-generated models. The time-consuming process of manually labeling training data can be avoided by generating the training data. Alternatively, creating samples with a stained binder that shows contrast in the scan can be used, but requires the production of special samples, which can be complex and expensive. The method presented here can be easily adapted to other kinds of material by adjusting the training data.

3.6. Core Reference

- A. Grießer, R. Westerteiger, E. Glatt, H. Hagen, and A. Wiegmann, “Deep learning based segmentation of binder and fibers in gas diffusion layers,” *Next Materials*, vol. 6, p. 100411, 2025. DOI: 10.1016/j.nxmater.2024.100411

4. Fiber length determination for injection molded glass fiber reinforced composite materials

Contents

4.1. Abstract	43
4.2. Introduction	44
4.3. Related Work	44
4.4. Approach	45
4.5. Results	49
4.5.1. Conclusion	51
4.6. Core Reference	51

4.1. Abstract

Fiber length is a crucial measure for fibrous materials such as composites or nonwovens, as it influences many critical material properties. Traditional experimental methods to determine fiber length involve significant efforts, are time-consuming, and prone to user-bias effects. In comparison, assessing fiber length distributions on a CT scan is a novel approach that allows easy, reproducible, and exact measurements of this crucial material property. Furthermore, determining fiber lengths based on a CT scan is a non-destructive analysis method. This not only allows analyzing a freshly manufactured sample, but it is also possible to examine the same sample again after a certain length of usage to investigate the aging of the material (e.g., changes in the fiber length distribution, the matrix, or various other parameters). This chapter presents the process of obtaining fiber length statistics starting from a micro-computed tomography (micro-CT) scan. On a GF/PA6 injection molding sample, the digital fiber length determination results are compared to a traditionally obtained fiber length distribution, which was determined using the "FASEP" apparatus by "IDM Systems"¹.

¹<http://www.fasep.biz/fasepfamily.html>

4.2. Introduction

Fibrous materials are essential in industries such as lightweight automotive materials [40] [71], filtration [41], and hygiene products [42]. The properties of these materials depend on microstructural geometric statistics, making the analysis of individual fibers a powerful tool in material engineering. Fiber length, for example, is a fundamental parameter influencing material properties in composites and nonwovens. Traditional methods for determining fiber length are labor-intensive, prone to user bias, and time-consuming. In contrast, CT-scan-based approaches offer a novel, non-destructive, and reproducible method to assess fiber length distribution. These digital techniques enable the easy analysis of freshly manufactured samples and their re-examination after use to investigate material aging, including changes in fiber length, the matrix, or other components. In this work, I present a method to measure fiber length in micro-CT scans and compare it to an established experimental method. The used example is shown in Figure 4.1.

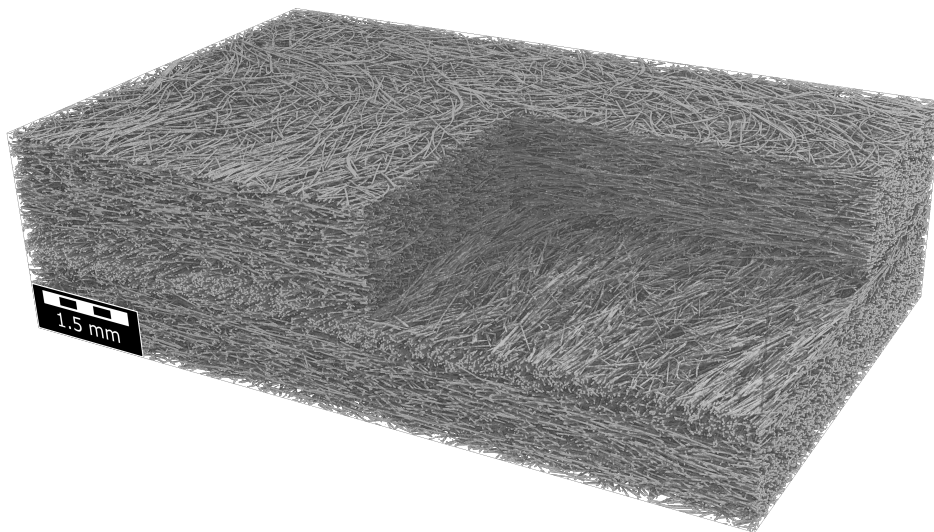


Figure 4.1.: *Rendering of a PP-LGF30 sample after CT scanning and segmentation. This sample will be used for fiber length determination in this work. A section has been cut out to give more detailed insights into the structure.*

4.3. Related Work

Advancements in volumetric 3D scanning, such as micro-CT, have enabled detailed analysis of fiber-based materials over the past 15 years [44] [45]. These technologies provide valuable insights into materials, provided the resolution and field of view are sufficient for statistical relevance. Analyzing large 3D scans of fibrous materials is challenging due to the amount of data that needs to be processed. Composite materials typically have straight, densely packed

fibers, while nonwovens feature curved, low-density fibers. This variation necessitates efficient algorithms capable of handling a wide range of geometries and large enough structures to capture representative elementary volumes (REV). While some methods compute fiber orientation using image-based approaches [12], [13], my study focuses on identifying and representing individual fibers analytically with piecewise linear trajectories and cross-sectional parameters. Prior approaches to fiber segmentation include skeletonization methods [16] [17], orientation gradient analysis [18], and deep learning [19] [21]. However, machine learning-based methods often require labor-intensive manual labeling. The approach presented in this work circumvents this by generating synthetic training data using the "FiberGeo" [69] module in "GeoDict" [27] allowing flexibility to model diverse fibrous materials. This technique supports the efficient computation of geometric properties, such as fiber length distribution, and the creation of accurate material models [3], [4]. My method is scalable to industrial dimensions, enabling material property analysis relevant to patents [51]. Another approach to measuring fiber length in micro-CT scans that does not rely on single fiber identification is presented by Kroneberg et al. [14]. They detect fiber endpoints based on the surface curvature and then use them to estimate the fiber length based on an approach presented by Kuhlmann and Redenbach [15]. This method is limited to straight fibers only.

4.4. Approach

In the conducted work, two different paths were followed to determine a fiber length distribution. First, a standard experimental determination of fiber length was employed. In the novel approach, digital fiber length measurement based on CT scanning and AI-based instant segmentation of single fibers was used. The used example is from the joint research project "DigiLaugBeh"². In this project, the project partners aim at a digital development of a lye container for washing machines made from PP-LGF30 (Polypropylene with 30 wt.-% of long glass fibers with a fiber diameter of 16.2 μm). For the experimental setup, PP-LGF30 was injected into a spiral mold, and samples were cut at multiple positions. Those samples were then scanned for digital analysis. The scans were conducted on a v|tome|x m 300180 Metrology Edition by GE Sensing & Inspection Technologies. The scan resolution was 3.3 μm . The overall scan size was 3101 x 834 x 2963 voxels. The "FASEP"³ method used for experimental analysis involves multiple steps according to ISO / DIS 22314 [72]. First, ashing was performed to remove the composite matrix and isolate the fibers. This was followed by a dilution process, ensuring that fibers could be individually analyzed under a microscope. Finally, microscopic analysis provided detailed insights into fiber length distribution. While effective, this process is labor-intensive and relies heavily on correct physical sample preparation. For the digital method, the CT-scan (Figure 4.2) was processed (e.g.,

²<https://www.math2market.com/math2market/publicly-funded-projects/digilaugbeh.html>

³<http://www.fasep.biz/fasepfamily.html>

cropping, rotation, and/or alignment) as the starting point to obtain the fiber length distribution, and its quality was improved through image filters. The resulting dataset is segmented into fibers, pores, and matrix by AI segmentation, depending on the contrast between the material components.

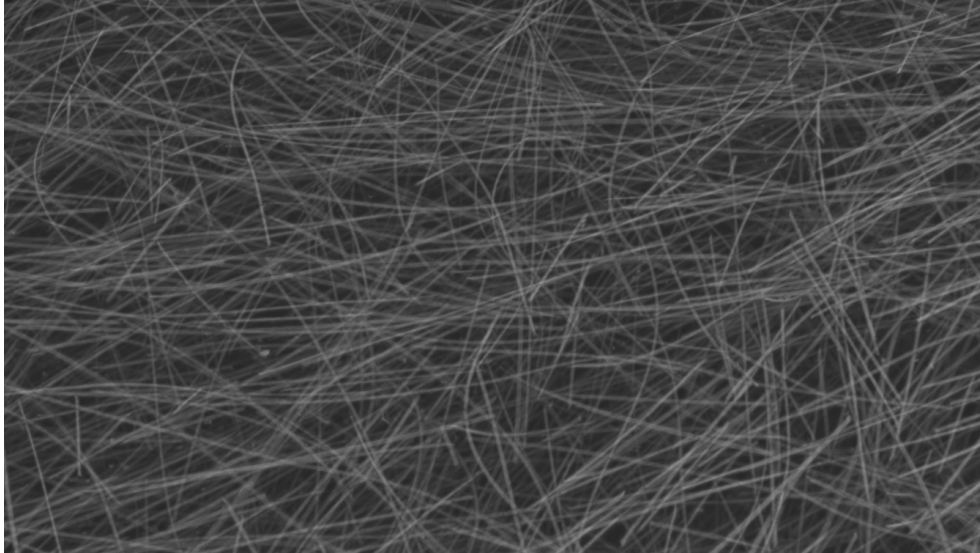


Figure 4.2.: *CT scan before analysis*

The segmentation of individual fibers and determining their length are completed using the method presented in Grießer et al. [6] (see Chapter 2), which was adapted for long fiber reinforced polymer composites. While the core method presented was preserved, some steps were adapted to achieve a better performance on a broader range of datasets. Similar to the original method, a neural network in the 3D U-NET architecture [53], [70] is trained using a sliding window approach. In comparison to the original method, the window size was increased to 52 by 52 by 52 Voxels to capture more of a fiber's topology. The training data was created artificially using GeoDict's fiber generator, FiberGeo. For these artificial structures, the centerline of each fiber is known. The amount of training data was massively increased compared to the original method, where only nine structures, each of size 512 by 512 by 256 voxels, were used for training (example in Figure 4.3). 100 structures, each 800 by 800 by 800 voxels, were used to train the neural network for 3 weeks on a Nvidia GeForce 4090 GPU. The training dataset contained a much wider range of fiber diameters from 4 to 40 voxels. Variations in diameter along the trajectory of a single fiber were also introduced, and slightly elliptical fibers were included to make the network more robust. Additionally, the orientation of the fibers was changed from being in the x-y plane to isotropic to remove the strong orientation dependency of the original method. Finally, surface roughness in varying strengths was added to the fibers.

The neural network trained with these training datasets is able to detect the centerlines reliably in a much wider range of datasets. Figure 4.4 shows how the improved neural network performs on an example of three mostly

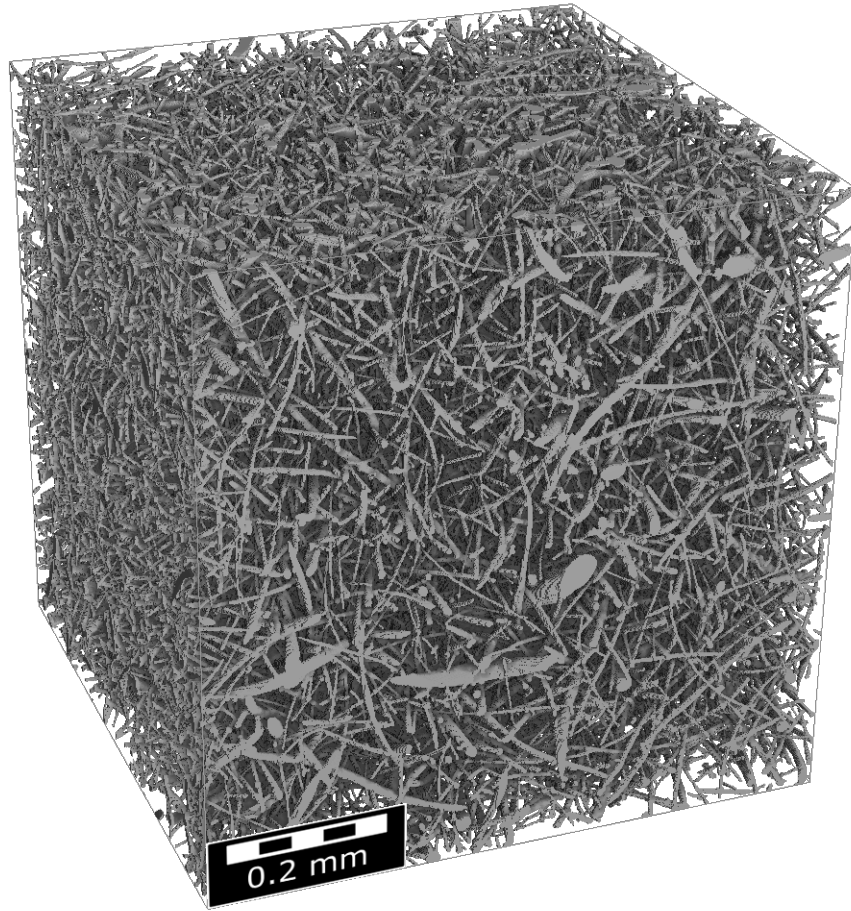


Figure 4.3.: *One example training structure containing a solid volume fraction of 9.1% of isotropically oriented fibers*

straight entangled glass fibers taken from a glass wool sample. Results from a morphological skeletonization [73] and distance transform-based approach are compared and show the advantage of the neural network-based approach.

The identified centerlines are used to determine the trajectories of the individual fibers. This is done by first skeletonizing the output of the neural network using the morphological skeletonizer from Palagyi et al. [73], to get the centerlines down to one voxel diameter. The centerline voxels are translated into a graph data structure where every centerline voxel with only one or more than two neighboring voxels is transformed into a node, and the voxels with exactly two neighboring voxels make up the edges between the node voxels. This structure is then used to resolve crossings that might happen if the centerline is touching due to very thin fibers. Cases where the centerline might fall apart due to errors made by the neural network are also handled by reconnecting fragments of fibers.

When fiber fragments are found, endpoint pairs are analyzed according to

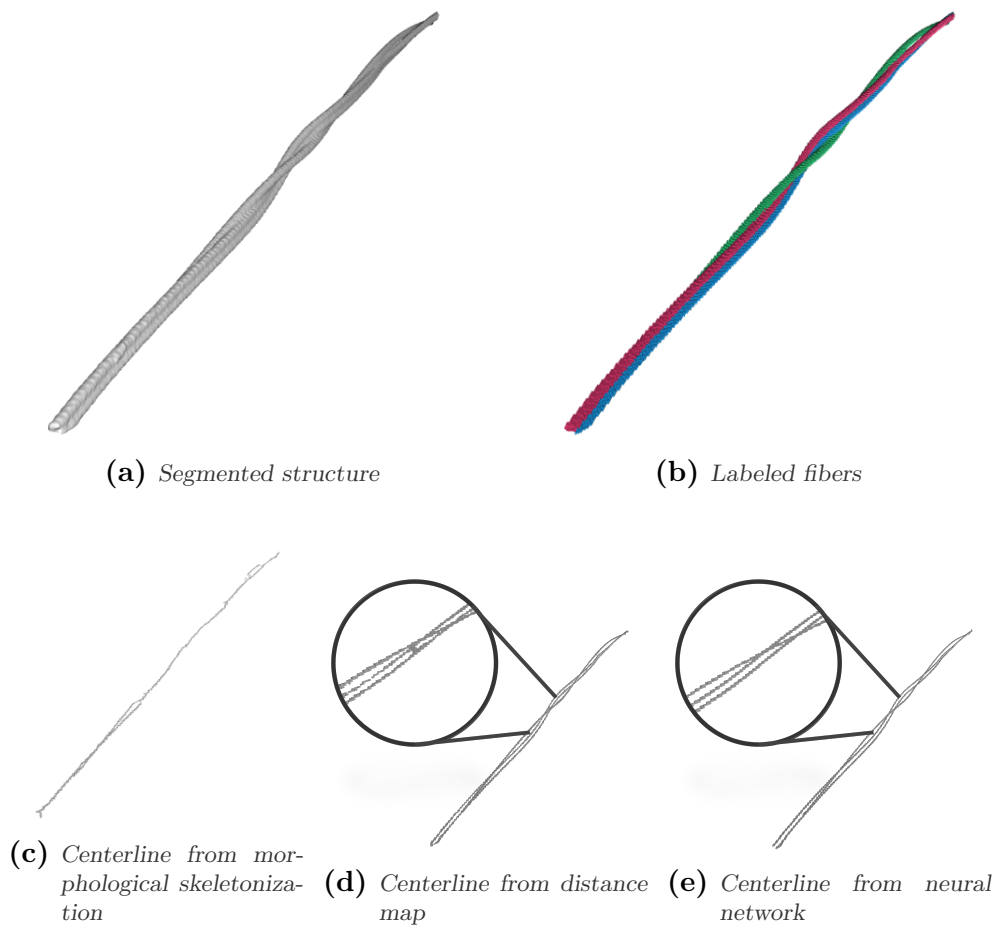


Figure 4.4.: Example of how the improved neural network performs on glass fibers from a glass wool sample. Figure 4.4c shows a morphological skeletonization. Figure 4.4d shows a distance transform-based approach. Both approaches perform worse than the neural network-based approach presented in this work, shown in Figure 4.4e

their distance, orientation, and the orientation of the connecting piece between them. At the end of this process, the graph is decomposed into a list of simple graphs only containing a starting point, an endpoint, and a list of voxels that make up the centerline of one fiber between them. This list is decimated using the Douglas–Peucker algorithm [74] and then used to construct analytical representations of the fibers using a distance transform to measure the fiber diameter at each point remaining after the decimation. Finally, a watershed algorithm was used to label each voxel in the original image according to the ID of its centerline (Figure 4.5).

To validate the performance of the improved neural network, I ran the same validation structures presented in Grieser et al. [6]. The ground truth is known for these artificially generated structures, and it is possible to check if any fibers were split up or merged with another fiber. These validations give



Figure 4.5.: Identified single fibers in the CT-scan are marked by color coding

Number of fibers	Validation 1		Validation 2		Validation 3	
	Absolute	Relative	Absolute	Relative	Absolute	Relative
	221		407		339	
Errors old method	13	5.9%	33	8.1%	17	5%
Errors new method	16	7.2%	13	3.2%	5	1.5%

Table 4.1.: Performance of the enhanced neural network compared to the original network presented in Table 2.2

a good measurement of the method’s best performance, as the neural network is expected to perform better on the artificially generated structures than on real samples that may contain additional artifacts (Table 4.1).

While the first validation structure has a slight increase in errors, the other two significantly improved, bringing the results closer to the ground truth.

4.5. Results

I applied my method to a PP-LGF30 sample produced and scanned in the “DigiLaugBeh” project to compare it to the fiber length measurements computed with the FASEP system. The FASEP system’s measurements yielded a mean fiber length of 1628 μm . My method computed a mean fiber length of 1583 μm . It only deviates by 2.8% from the standardized measurement.

Figure 4.6 shows the fiber length histogram of the two methods. The digital

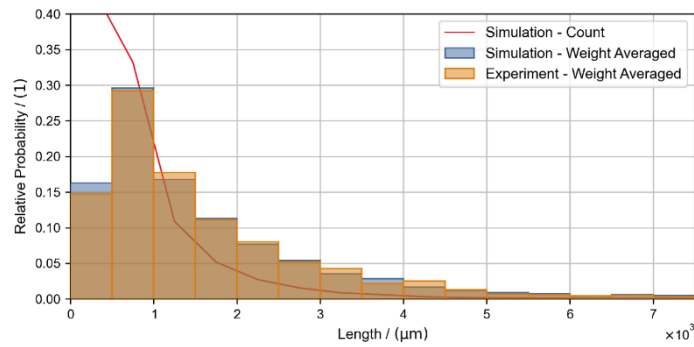


Figure 4.6.: Comparison of fiber length distribution obtained from experiment (orange) and digital analysis (blue)

calculation of the fiber length distribution using the centerlines of each fiber and the experimental determination of this measure shows a high correlation. This indicates that the method presented here not only performs well on the artificially generated validation structures but also transfers well to real-world micro-CT scans as long as the fibers are sufficiently resolved.

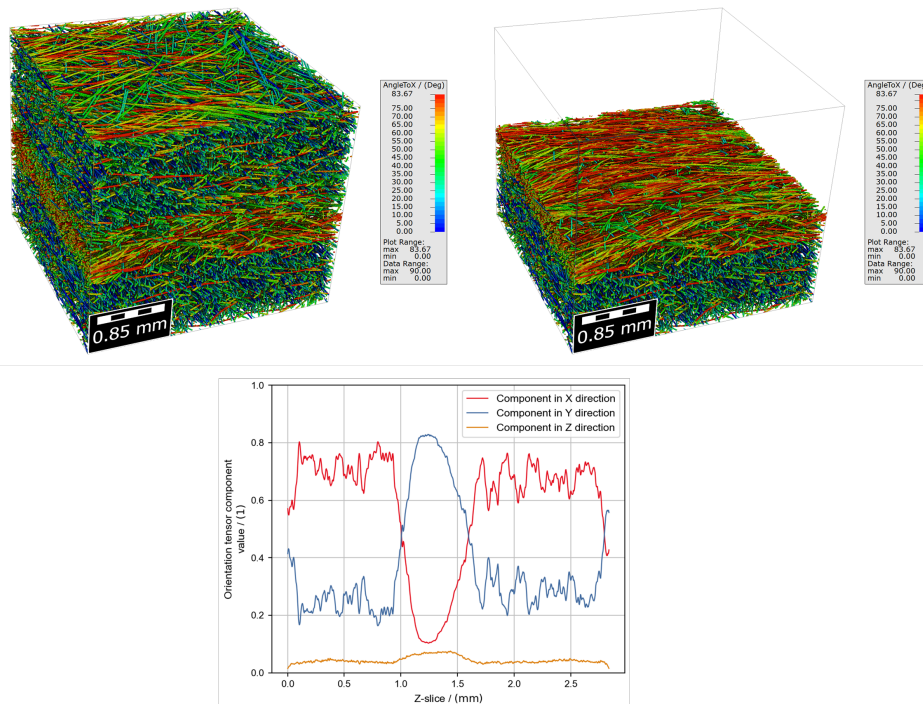


Figure 4.7.: Fiber orientation analysis on a crop of the PP-LGF30 sample. The two images on the top show the orientation in each fiber voxel encoded as the angle to the x-axis. The bottom image shows the three components of the fiber direction averaged for each slice in the z-direction.

The results emphasize the suitability and accuracy of this digital, AI-based, and non-destructive approach for determining the fiber length distribution in

composite materials. Further, my method directly computes the fiber orientation for each fiber (Figure 4.7). This analysis clearly shows the change in orientation that can visually be observed in the middle of the sample in Figure 4.1. The observed orientation profile is typical for an injection-molded sample, as the flow velocity in the center of the sample is higher, and higher temperature leads to lower viscosity in the center area, influencing the final fiber orientation.

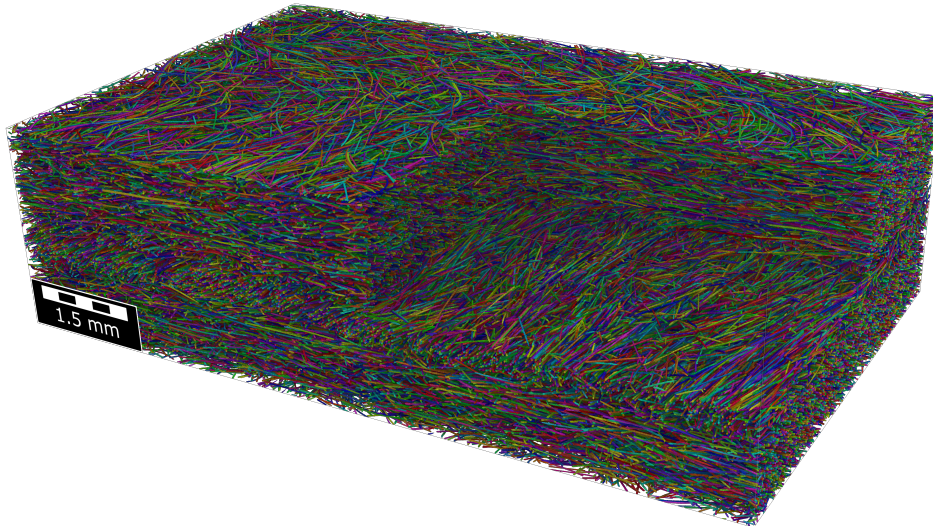


Figure 4.8.: Final result of the fiber identification with each fiber labeled in a different color

4.5.1. Conclusion

The method presented in this work can be used to determine fiber length and other geometrical fiber properties from micro-CT scans of composite materials. Classical methods that rely on destroying the samples can be accommodated or even replaced by this much less labor-intensive method. On top of this, the CT-based analysis allows more insights into the samples than just the fiber length. Compared to experimental methods, a lot of additional information can be obtained from just one scan. Orientations, fiber diameters, fiber shapes, or even the curvature of fibers can be computed on top of the fiber length. Spatial correlations of these parameters can be observed, such as fiber orientation variations through different material layers.

4.6. Core Reference

- A. Grießer, N. Nunheim, O. Rimmel, A. Blumer, H. Hagen, and A. Wiegmann, “Digital fiber length determination for injection molded glass fiber reinforced composite materials,” in *e-Journal of Nondestructive*

Testing: 14th Conference on Industrial Computed Tomography (iCT) 2025, vol. 30, Antwerpen, Belgium, Feb. 2025. DOI: 10.58286/30747

5. Conclusion

Extracting qualitative and quantitative measurements of microstructures from micro-computed tomography (micro-CT) scans is a complex and broad topic. This thesis presents approaches to this challenge for fibrous materials. The methods I presented utilize machine learning and artificially generated training data, building on preexisting structure generation methods. This way, the time-consuming and costly manual labeling of training data can be avoided, and the techniques can easily be adapted for different materials.

In Chapter 2, I presented a method for labeling individual fibers in micro-CT scans of nonwoven materials typically used in the hygiene industry. A convolutional neural network was trained to find the centerlines of fibers. The training data was obtained from artificially generated nonwovens where the centerline of each fiber was known from the generation process. The centerlines found by the neural network were then used to label the individual fibers and build analytical representations for each fiber. Using these representations, geometrical properties for each fiber were successfully extracted and analyzed to compare structures that were manufactured using different processes.

In Chapter 3, I adapted the approach to label material phases in micro-CT scans instead of individual objects. The material investigated was carbon paper used as gas diffusion layers in fuel cells. In micro-CT scans of these materials, there is usually no contrast between binder and fibers, and segmenting these two phases is challenging. To overcome this, a convolutional neural network was trained on artificially generated models of carbon paper, where the segmentation of fibers and binder is a result of the generation process. The neural network was then successfully used to segment fibers and binder in the micro-CT scans of real samples.

Finally, in Chapter 4, the method from Chapter 2 was refined for application on composite materials instead of nonwovens. Composites pose different challenges for fiber labeling compared to nonwovens. In the nonwoven from Chapter 2, the fibers are not very dense but very long and have complex trajectories. In comparison, the fibers in composites are usually very simple: mostly straight, but densely packed. The method was adapted by using different training data, eliminating constraints in orientation and fiber diameters. This was then used to evaluate the fiber length distribution in the composites and compare the results with an experimental approach. The neural network-based method successfully measures fiber length distributions similar to those of the experimental approach while also yielding additional measurements such as fiber diameters and orientation.

Using artificially generated microstructures to train neural networks for image analysis tasks is a powerful tool for gaining insights into materials. The

approaches presented in this thesis showcase how different challenges can be tackled using this core idea. The insights gained from this kind of analysis can then be used to enable digital material engineering for faster and more sustainable iterative design of materials.

Bibliography

- [1] S. A. Mäkiharju, J. Dewanckele, M. Boone, C. Wagner, and A. Griesser, “Tomographic x-ray particle tracking velocimetry: Proof-of-concept in a creeping flow,” *Experiments in Fluids*, vol. 63, pp. 1–12, 2022. DOI: 10.1007/s00348-021-03362-w.
- [2] A. Grießer, M. Hümbert, S. Rief, W. De Boever, and L. Hunter, “Metal foams: Linking dynamic ct results to simulation and modeling,” *Microscopy and Microanalysis*, vol. 27, no. S1, pp. 1032–1033, 2021. DOI: 10.1017/S1431927621003901.
- [3] M. Weber, A. Grießer, D. Mosbach, E. Glatt, A. Wiegmann, and V. Schmidt, “Copula-based modeling and simulation of 3d systems of curved fibers by isolating intrinsic fiber properties and external effects,” *Scientific Reports*, vol. 13, no. 1, p. 19 359, 2023. DOI: 10.1038/s41598-023-46644-5.
- [4] M. Weber, A. Grießer, E. Glatt, A. Wiegmann, and V. Schmidt, “Modeling curved fibers by fitting r-vine copulas to their frenet representations,” *Microscopy and Microanalysis*, vol. 29, no. 1, pp. 155–165, 2023. DOI: 10.1093/micmic/ozac030.
- [5] M. Weber, A. Grießer, D. Mosbach, E. Glatt, A. Wiegmann, and V. Schmidt, “Investigating microstructure–property relationships of non-wovens by model-based virtual material testing,” *Transport in Porous Media*, vol. 151, no. 6, pp. 1403–1421, 2024. DOI: 10.1007/s11242-024-02079-8.
- [6] A. Grießer, R. Westerteiger, E. Glatt, H. Hagen, and A. Wiegmann, “Identification and analysis of fibers in ultra-large micro-ct scans of non-woven textiles using deep learning,” *The Journal of The Textile Institute*, vol. 114, no. 11, pp. 1647–1657, 2023. DOI: 10.1080/00405000.2022.2145429.
- [7] A. Grießer, R. Westerteiger, C. Wagner, H. Hagen, and A. Wiegmann, “Machine learning-based single fiber extraction from micro-ct scans with geodict,” in *8th Conference on Industrial Computed Tomography (iCT) 2018*, vol. 23, Wels, Austria, Feb. 2018. [Online]. Available: <https://www.ndt.net/?id=21922>.
- [8] A. Grießer, R. Westerteiger, C. Wagner, and A. Wiegmann, “Fiberfind: Machine learning-based segmentation and identification of individual fibers in ct images of fibrous media,” in *International Conference on Tomography of Materials & Structures*, 2019.

- [9] A. Griebner, R. Westerteiger, E. Glatt, H. Hagen, and A. Wiegmann, "Deep learning based segmentation of binder and fibers in gas diffusion layers," *Next Materials*, vol. 6, p. 100411, 2025. DOI: [10.1016/j.nxmte.2024.100411](https://doi.org/10.1016/j.nxmte.2024.100411).
- [10] A. Griebner, N. Nunheim, O. Rimmel, A. Blumer, H. Hagen, and A. Wiegmann, "Digital fiber length determination for injection molded glass fiber reinforced composite materials," in *e-Journal of Nondestructive Testing: 14th Conference on Industrial Computed Tomography (iCT) 2025*, vol. 30, Antwerpen, Belgium, Feb. 2025. DOI: [10.58286/30747](https://doi.org/10.58286/30747).
- [11] M. Hümbert, O. Rimmel, and A. Griebner, "Analysis of fibers, pores, and mechanical properties in μ ct-scan of a long fiber-reinforced thermoplastic," *Microscopy and Microanalysis*, vol. 28, no. S1, pp. 262–264, 2022. DOI: [10.1017/S1431927622001866](https://doi.org/10.1017/S1431927622001866).
- [12] M. Axelsson, "Estimating 3d fibre orientation in volume images," vol. 2008, Jan. 2009, pp. 1–4. DOI: <https://doi.org/10.1109/ICPR.2008.4761631>.
- [13] M. Krause, J. Hausherr, B. Burgeth, C. Herrmann, and W. Krenkel, "Determination of the fibre orientation in composites using the structure tensor and local x-ray transform," *Journal of Materials Science*, vol. 45, pp. 888–896, Feb. 2010. DOI: <https://doi.org/10.1007/s10853-009-4016-4>.
- [14] M. Kronenberger, K. Schladitz, O. Wirjadi, C. Weber, B. Hamann, and H. Hagen, "Endpoint detection of partially overlapping straight fibers using high positive gaussian curvature in 3d images," *Image Analysis and Stereology*, vol. 38, no. 3, pp. 245–253, Dec. 2019. DOI: [10.5566/ias.2197](https://doi.org/10.5566/ias.2197). [Online]. Available: <https://www.ias-iss.org/ojs/IAS/article/view/2197>.
- [15] M. Kuhlmann and C. Redenbach, "Estimation of Fibre Length Distributions from Fibre Endpoints," *Scandinavian Journal of Statistics*, vol. 42, no. 4, pp. 1010–1022, Dec. 2015. [Online]. Available: <https://ideas.repec.org/a/bla/scjsta/v42y2015i4p1010-1022.html>.
- [16] P. Henyš and L. Čapek, "Individual yarn fibre extraction from microct: Multilevel machine learning approach," *The Journal of The Textile Institute*, vol. 0, no. 0, pp. 1–8, 2021. DOI: <https://doi.org/10.1080/00405000.2020.1865503>. eprint: <https://doi.org/10.1080/00405000.2020.1865503>. [Online]. Available: <https://doi.org/10.1080/00405000.2020.1865503>.
- [17] X. Huang, D. Wen, Y. Zhao, Q. Wang, W. Zhou, and D. Deng, "Skeleton-based tracing of curved fibers from 3d x-ray microtomographic imaging," *Results in Physics*, vol. 6, pp. 170–177, 2016, ISSN: 2211-3797. DOI: <https://doi.org/10.1016/j.rinp.2016.03.008>. [Online]. Available: <https://www.sciencedirect.com/science/article/pii/S221137971600036X>.

-
- [18] J. Viguié, P. Latil, L. Orgéas, P. Dumont, S. Rolland du Roscoat, J.-F. Bloch, C. Marulier, and O. Guiraud, “Finding fibres and their contacts within 3d images of disordered fibrous media,” *Composites Science and Technology*, vol. 89, pp. 202–210, 2013, ISSN: 0266-3538. DOI: <https://doi.org/10.1016/j.compscitech.2013.09.023>. [Online]. Available: <https://www.sciencedirect.com/science/article/pii/S0266353813003850>.
- [19] A. Badran, D. Marshall, Z. Legault, R. Makovetsky, B. Provencher, N. Piché, and M. Marsh, “Automated segmentation of computed tomography images of fiber-reinforced composites by deep learning,” *Journal of Materials Science*, vol. 55, pp. 1–17, Dec. 2020. DOI: <https://doi.org/10.1007/s10853-020-05148-7>.
- [20] D. Depriester, S. Rolland du Roscoat, L. Orgéas, C. Geindreau, B. Levraud, and F. Brémond, “Individual fibre separation in 3d fibrous materials imaged by x-ray tomography,” *Journal of Microscopy*, vol. 286, no. 3, pp. 220–239, 2022. eprint: <https://onlinelibrary.wiley.com/doi/pdf/10.1111/jmi.13096>. [Online]. Available: <https://onlinelibrary.wiley.com/doi/abs/10.1111/jmi.13096>.
- [21] T. Konopczyński, T. Kröger, L. Zheng, and J. Hesser, *Instance segmentation of fibers from low resolution ct scans via 3d deep embedding learning*, 2019. arXiv: 1901.01034 [cs.CV].
- [22] P. Westenberger, P. Estrade, and D. Lichau, “Fibre orientation visualization with avizofire,” *NDTnet*, 2012. [Online]. Available: <https://www.ndt.net/search/docs.php3?id=13711#>.
- [23] H. Kallel and K. Joulain, “Design and thermal conductivity of 3d artificial cross-linked random fiber networks,” *Materials & Design*, vol. 220, p. 110 800, 2022, ISSN: 0264-1275. DOI: <https://doi.org/10.1016/j.matdes.2022.110800>. [Online]. Available: <https://www.sciencedirect.com/science/article/pii/S0264127522004221>.
- [24] I. Arganda-Carreras, V. Kaynig, C. Rueden, K. W. Eliceiri, J. Schindelin, A. Cardona, and H. Sebastian Seung, “Trainable weka segmentation: A machine learning tool for microscopy pixel classification,” *Bioinformatics (Oxford, England)*, vol. 33, no. 15, pp. 2424–2426, Aug. 2017, ISSN: 1367-4803. DOI: 10.1093/bioinformatics/btx180. [Online]. Available: <https://doi.org/10.1093/bioinformatics/btx180>.
- [25] J. Phan, L. C. Ruspini, and F. Lindseth, “Automatic segmentation tool for 3d digital rocks by deep learning,” *Scientific Reports*, vol. 11, no. 1, p. 19 123, Sep. 2021, ISSN: 2045-2322. DOI: 10.1038/s41598-021-98697-z. [Online]. Available: <https://doi.org/10.1038/s41598-021-98697-z>.
- [26] S. Karimpouli and P. Tahmasebi, “Segmentation of digital rock images using deep convolutional autoencoder networks,” *Computers Geosciences*, vol. 126, pp. 142–150, 2019, ISSN: 0098-3004. DOI: <https://doi.org/10.1016/j.cogsci.2019.07.011>.

- doi.org/10.1016/j.cageo.2019.02.003. [Online]. Available: <https://www.sciencedirect.com/science/article/pii/S0098300418303911>.
- [27] J. Becker, F. Biebl, B. M., L. Cheng, *et al.*, *Geodict software*, 2022.
- [28] K. Tang, Q. Meyer, R. White, R. T. Armstrong, P. Mostaghimi, Y. Da Wang, S. Liu, C. Zhao, K. Regenauer-Lieb, and P. K. M. Tung, “Deep learning for full-feature x-ray microcomputed tomography segmentation of proton electron membrane fuel cells,” *Computers Chemical Engineering*, vol. 161, p. 107768, 2022, ISSN: 0098-1354. DOI: <https://doi.org/10.1016/j.compchemeng.2022.107768>. [Online]. Available: <https://www.sciencedirect.com/science/article/pii/S0098135422001090>.
- [29] M. Mahdaviara, M. J. Shojaei, J. Siavashi, M. Sharifi, and M. J. Blunt, “Deep learning for multiphase segmentation of x-ray images of gas diffusion layers,” *Fuel*, vol. 345, p. 128180, 2023, ISSN: 0016-2361. DOI: <https://doi.org/10.1016/j.fuel.2023.128180>. [Online]. Available: <https://www.sciencedirect.com/science/article/pii/S0016236123007937>.
- [30] C. Chen and Y. Gao, “Using multi-threshold non-local means joint distribution method to analysis the spatial distribution patterns of binder and fibers in gas diffusion layers of fuel cells,” *Applied Energy*, vol. 358, p. 122513, 2024, ISSN: 0306-2619. DOI: <https://doi.org/10.1016/j.apenergy.2023.122513>. [Online]. Available: <https://www.sciencedirect.com/science/article/pii/S0306261923018779>.
- [31] S. Simaafrookhteh, R. Taherian, and M. Shakeri, “Stochastic microstructure reconstruction of a binder/carbon fiber/expanded graphite carbon fiber paper for pemfcs applications: Mass transport and conductivity properties,” *Journal of The Electrochemical Society*, vol. 166, pp. 3287–3299, May 2019. DOI: 10.1149/2.0331907jes.
- [32] S. Hein, T. Danner, D. Westhoff, B. Prifling, *et al.*, “Influence of conductive additives and binder on the impedance of lithium-ion battery electrodes: Effect of morphology,” *Journal of The Electrochemical Society*, vol. 167, no. 1, p. 013546, Jan. 2020. DOI: 10.1149/1945-7111/ab6b1d. [Online]. Available: <https://dx.doi.org/10.1149/1945-7111/ab6b1d>.
- [33] B. L. Trembacki, A. N. Mistry, D. R. Noble, M. E. Ferraro, P. P. Mukherjee, and S. A. Roberts, “Editors’ choice—mesoscale analysis of conductive binder domain morphology in lithium-ion battery electrodes,” *Journal of The Electrochemical Society*, vol. 165, no. 13, E725, Oct. 2018. DOI: 10.1149/2.0981813jes. [Online]. Available: <https://dx.doi.org/10.1149/2.0981813jes>.
- [34] X. Wang, Z. Qu, T. Lai, G. Ren, and W. Wang, “Enhancing water transport performance of gas diffusion layers through coupling manipulation of pore structure and hydrophobicity,” *Journal of Power Sources*, vol. 525, p. 231121, 2022, ISSN: 0378-7753. DOI: <https://doi.org/10.1016/j.jpowsour.2022.231121>.

- 1016/j.jpowsour.2022.231121. [Online]. Available: <https://www.sciencedirect.com/science/article/pii/S0378775322001446>.
- [35] R. Flückiger, S. A. Freunberger, D. Kramer, A. Wokaun, G. G. Scherer, and F. N. Büchi, “Anisotropic, effective diffusivity of porous gas diffusion layer materials for pefc,” *Electrochimica Acta*, vol. 54, no. 2, pp. 551–559, 2008, ISSN: 0013-4686. DOI: <https://doi.org/10.1016/j.electacta.2008.07.034>. [Online]. Available: <https://www.sciencedirect.com/science/article/pii/S0013468608008864>.
- [36] A. G. Yiotis, M. E. Kainourgiakis, G. C. Charalambopoulou, and A. K. Stubos, “Microscale characterisation of stochastically reconstructed carbon fiber-based gas diffusion layers; effects of anisotropy and resin content,” *Journal of Power Sources*, vol. 320, pp. 153–167, 2016, ISSN: 0378-7753. [Online]. Available: <https://www.sciencedirect.com/science/article/pii/S0378775316304694>.
- [37] N. Zamel, J. Becker, and A. Wiegmann, “Estimating the thermal conductivity and diffusion coefficient of the microporous layer of polymer electrolyte membrane fuel cells,” *Journal of Power Sources*, vol. 207, pp. 70–80, 2012, ISSN: 0378-7753. DOI: <https://doi.org/10.1016/j.jpowsour.2012.02.003>. [Online]. Available: <https://www.sciencedirect.com/science/article/pii/S0378775312003047>.
- [38] H. B. Harandi, A. Asadi, H. Fathi, and P.-C. Sui, “Combined macroscopic and pore scale modeling of direct contact membrane distillation with micro-porous hydrophobic membranes,” *Desalination*, vol. 514, p. 115 171, 2021, ISSN: 0011-9164. DOI: <https://doi.org/10.1016/j.desal.2021.115171>. [Online]. Available: <https://www.sciencedirect.com/science/article/pii/S0011916421002423>.
- [39] K. Schladitz, S. Peters, D. Reinel-Bitzer, A. Wiegmann, and J. Ohser, “Design of acoustic trim based on geometric modeling and flow simulation for non-woven,” *Computational Materials Science*, vol. 38, no. 1, pp. 56–66, 2006, ISSN: 0927-0256. DOI: <https://doi.org/10.1016/j.commatsci.2006.01.018>. [Online]. Available: <https://www.sciencedirect.com/science/article/pii/S092702560600019X>.
- [40] D. May, B. Willenbacher, J. Semar, K. Sharp, and P. Mitschang, “Out-of-plane permeability of 3d woven fabrics for composite structures,” *The Journal of The Textile Institute*, vol. 111, no. 7, pp. 1047–1053, 2020. DOI: <https://doi.org/10.1080/00405000.2019.1682759>. eprint: <https://doi.org/10.1080/00405000.2019.1682759>. [Online]. Available: <https://doi.org/10.1080/00405000.2019.1682759>.
- [41] K. M. Hoess, F. J. Hahn, S. Schmauder, and F. Keller, “Predicting the mechanical behavior of a polypropylene-based nonwoven using 3d microstructural simulation,” *The Journal of The Textile Institute*, vol. 0, no. 0, pp. 1–12, 2021. DOI: <https://doi.org/10.1080/00405000.2021.2001891>. eprint: <https://doi.org/10.1080/00405000.2021.2001891>.

- [Online]. Available: <https://doi.org/10.1080/00405000.2021.2001891>.
- [42] A. J. Rigby, S. C. Anand, and A. R. Horrocks, "Textile materials for medical and healthcare applications," *The Journal of The Textile Institute*, vol. 88, no. 3, pp. 83–93, 1997. DOI: <https://doi.org/10.1080/00405009708658589>. eprint: <https://doi.org/10.1080/00405009708658589>. [Online]. Available: <https://doi.org/10.1080/00405009708658589>.
- [43] B. Pourdeyhimi and R. Ramanathan, "Image analysis method for estimating 2-d fiber orientation and fiber length in discontinuous fiber reinforced composites," *Polymers and Polymer Composites*, vol. 3, no. 4, pp. 277–87, 1995.
- [44] L. Suragani Venu, E. Shim, N. Anantharamaiah, and B. Pourdeyhimi, "Three-dimensional structural characterization of nonwoven fabrics," *Microscopy and microanalysis : the official journal of Microscopy Society of America, Microbeam Analysis Society, Microscopical Society of Canada*, vol. 18, pp. 1–12, Dec. 2012. DOI: <https://doi.org/10.1017/S143192761201375X>.
- [45] P. Soltani, M. Johari, and M. Zarrebini, "3d fiber orientation characterization of nonwoven fabrics using x-ray micro-computed tomography," *World Journal of Textile Engineering and Technology*, pp. 41–47, Jan. 2016.
- [46] I. Davoodi Kermani, M. Schmitter, J. F. Eichinger, R. C. Aydin, and C. J. Cyron, "Computational study of the geometric properties governing the linear mechanical behavior of fiber networks," *Computational Materials Science*, vol. 199, p. 110 711, 2021, ISSN: 0927-0256. DOI: <https://doi.org/10.1016/j.commatsci.2021.110711>. [Online]. Available: <https://www.sciencedirect.com/science/article/pii/S0927025621004389>.
- [47] I. P. Beckman, G. Berry, H. Cho, and G. Riveros, "Digital twin geometry for fibrous air filtration media," *Fibers*, vol. 9, no. 12, 2021, ISSN: 2079-6439. DOI: <https://doi.org/10.3390/fib9120084>. [Online]. Available: <https://www.mdpi.com/2079-6439/9/12/84>.
- [48] P. Townsend, E. Larsson, T. Karlson, S. A. Hall, *et al.*, "Stochastic modelling of 3d fiber structures imaged with x-ray microtomography," *Computational Materials Science*, vol. 194, p. 110 433, 2021, ISSN: 0927-0256. DOI: <https://doi.org/10.1016/j.commatsci.2021.110433>. [Online]. Available: <https://www.sciencedirect.com/science/article/pii/S0927025621001580>.
- [49] J. Hilden, S. Rief, and B. Planas, "Fibergeo user guide 2022," Tech. Rep., Aug. 2021. DOI: <https://doi.org/10.30423/userguide.geodict2022-fibergeo>.
- [50] J. Becker, F. Biebl, L. Cheng, E. Glatt, *et al.*, *Geodict software*, Sep. 2021. [Online]. Available: https://www.math2market.de/GeoDict/geodict_download.php.

-
- [51] J. Kroutilova, M. Maas, Z. Mecl, T. Wagner, F. Klaska, and P. Kasparikova, “Bulky nonwoven fabric with enhanced compressibility and recovery,” pat. WO 2020/103964 A1, May 2020. [Online]. Available: <https://patents.google.com/patent/WO2020103964A1/en#patentCitations>.
- [52] Martín Abadi, Ashish Agarwal, Paul Barham, Eugene Brevdo, *et al.*, *Tensorflow: Large-scale machine learning on heterogeneous systems*, Software available from tensorflow.org, 2015. [Online]. Available: <https://www.tensorflow.org/>.
- [53] O. Ronneberger, P. Fischer, and T. Brox, “U-net: Convolutional networks for biomedical image segmentation,” in *Medical Image Computing and Computer-Assisted Intervention (MICCAI)*, ser. LNCS, (available on arXiv:1505.04597 [cs.CV]), vol. 9351, Springer, 2015, pp. 234–241. [Online]. Available: <http://lmb.informatik.uni-freiburg.de/Publications/2015/RFB15a>.
- [54] Ö. Çiçek, A. Abdulkadir, S. S. Lienkamp, T. Brox, and O. Ronneberger, *3d u-net: Learning dense volumetric segmentation from sparse annotation*, 2016. arXiv: 1606.06650 [cs.CV].
- [55] S. Beucher and C. Lantuéjoul, “Use of watersheds in contour detection,” vol. 132, Jan. 1979.
- [56] C. H and K. OJ, “The structure of paper. i the statistical geometry of ideal two dimensional fiber networks,” *Tappi Journal*, vol. 43(9), pp. 737–752, 1960.
- [57] D. H. Page, R. S. Seth, B. D. Jorda, and M. C. Barb, “Curl, crimps, kinks and microcompressions in pulp fibres - their origin, measurement and significance,” *Punton V (ed.) Papermaking raw materials, Trans. VIIIth Fund. Res. Symp. Oxford*, pp. 183–227, 1985.
- [58] A. Griebner, R. Westerteiger, E. Glatt, W. De Boever, H. Hagen, and A. Wiegmann, *Identified fibers and validation data for fiber identification*, 2022. DOI: 10.30423/data.math2market-2022-02.sample-c.fiberfind. [Online]. Available: <https://doi.org/10.30423/data.math2market-2022-02.sample-c.fiberfind>.
- [59] J. Becker, C. Wieser, S. Fell, and K. Steiner, “A multi-scale approach to material modeling of fuel cell diffusion media,” *International Journal of Heat and Mass Transfer*, vol. 54, no. 7, pp. 1360–1368, 2011, ISSN: 0017-9310. DOI: <https://doi.org/10.1016/j.ijheatmasstransfer.2010.12.003>. [Online]. Available: <https://www.sciencedirect.com/science/article/pii/S0017931010006824>.
- [60] V. Schulz, J. Becker, A. Wiegmann, P. Mukherjee, and C. Wang, “Modeling of two-phase behavior in the gas diffusion medium of pefcs via full morphology approach,” English (US), *Journal of the Electrochemical Society*, vol. 154, no. 4, B419–B426, 2007, ISSN: 0013-4651. DOI: 10.1149/1.2472547.

- [61] J. Becker, V. Schulz, and A. Wiegmann, "Numerical determination of two-phase material parameters of a gas diffusion layer using tomography images," *Journal of Fuel Cell Science and Technology*, vol. 5, no. 2, p. 021006, Apr. 2008, ISSN: 1550-624X. DOI: 10.1115/1.2821600. eprint: https://asmedigitalcollection.asme.org/electrochemical/article-pdf/5/2/021006/5895765/021006_1.pdf. [Online]. Available: <https://doi.org/10.1115/1.2821600>.
- [62] N. Zamel, X. Li, J. Becker, and A. Wiegmann, "Effect of liquid water on transport properties of the gas diffusion layer of polymer electrolyte membrane fuel cells," *International Journal of Hydrogen Energy*, vol. 36, no. 9, pp. 5466–5478, 2011, ISSN: 0360-3199. DOI: <https://doi.org/10.1016/j.ijhydene.2011.01.146>. [Online]. Available: <https://www.sciencedirect.com/science/article/pii/S0360319911002746>.
- [63] N. Zamel, X. Li, J. Shen, J. Becker, and A. Wiegmann, "Estimating effective thermal conductivity in carbon paper diffusion media," *Chemical Engineering Science*, vol. 65, no. 13, pp. 3994–4006, 2010, ISSN: 0009-2509. DOI: <https://doi.org/10.1016/j.ces.2010.03.047>. [Online]. Available: <https://www.sciencedirect.com/science/article/pii/S0009250910002083>.
- [64] J. Zhang, H. Zhang, J. Wu, and J. Zhang, "Chapter 2 - design and fabrication of pem fuel cell mea, single cell, and stack," in *Pem Fuel Cell Testing and Diagnosis*, J. Zhang, H. Zhang, J. Wu, and J. Zhang, Eds., Amsterdam: Elsevier, 2013, pp. 43–80, ISBN: 978-0-444-53688-4. DOI: <https://doi.org/10.1016/B978-0-444-53688-4.00002-4>. [Online]. Available: <https://www.sciencedirect.com/science/article/pii/B9780444536884000024>.
- [65] L. Cindrella, A. Kannan, J. Lin, K. Saminathan, Y. Ho, C. Lin, and J. Wertz, "Gas diffusion layer for proton exchange membrane fuel cells—a review," *Journal of Power Sources*, vol. 194, no. 1, pp. 146–160, 2009, XIth Polish Conference on Fast Ionic Conductors 2008, ISSN: 0378-7753. DOI: <https://doi.org/10.1016/j.jpowsour.2009.04.005>. [Online]. Available: <https://www.sciencedirect.com/science/article/pii/S0378775309006399>.
- [66] E. Antolini, R. R. Passos, and E. A. Ticianelli, "Effects of the cathode gas diffusion layer characteristics on the performance of polymer electrolyte fuel cells," *Journal of Applied Electrochemistry*, vol. 32, no. 4, pp. 383–388, 2002, ISSN: 1572-8838. DOI: 10.1023/A:1016329820273. [Online]. Available: <https://doi.org/10.1023/A:1016329820273>.
- [67] A. Pfrang, D. Veyret, F. Sieker, and G. Tsotridis, "X-ray computed tomography of gas diffusion layers of pem fuel cells: Calculation of thermal conductivity," *International Journal of Hydrogen Energy*, vol. 35, no. 8, pp. 3751–3757, 2010, ISSN: 0360-3199. DOI: <https://doi.org/10.1016/j.ijhydene.2010.01.085>. [Online]. Available: <https://www.sciencedirect.com/science/article/pii/S0360319910001564>.

-
- [68] M. Reiter, M. Erler, C. Kuhn, C. Gusenbauer, and J. Kastner, “Simct: A simulation tool for x-ray imaging,” in *e-Journal of Nondestructive Testing Vol. 21(2)*, 2016. [Online]. Available: <https://www.ndt.net/search/docs.php?id=18746>.
- [69] J. Hilden, S. Rief, and B. Planas, *Geodict 2023 user guide. fibergeo handbook*. 2023. DOI: doi.org/10.30423/userguide.geodict. [Online]. Available: <https://doi.org/10.30423/userguide.geodict>.
- [70] Ö. Çiçek, A. Abdulkadir, S. S. Lienkamp, T. Brox, and O. Ronneberger, “3d u-net: Learning dense volumetric segmentation from sparse annotation,” in *Medical Image Computing and Computer-Assisted Intervention – MICCAI 2016*, S. Ourselin, L. Joskowicz, M. R. Sabuncu, G. Unal, and W. Wells, Eds., Cham: Springer International Publishing, 2016, pp. 424–432, ISBN: 978-3-319-46723-8.
- [71] U. N. Marathe and J. Bijwe, “High performance polymer composites - influence of processing technique on the fiber length and performance properties,” *Wear*, vol. 446-447, p. 203 189, 2020, ISSN: 0043-1648. DOI: <https://doi.org/10.1016/j.wear.2020.203189>. [Online]. Available: <https://www.sciencedirect.com/science/article/pii/S0043164819315716>.
- [72] “Plastics - glass-fibre-reinforced products - determination of fibre length,” International Organization for Standardization, Standard, 2023.
- [73] K. Palàgyi and A. Kuba, “A 3d 6-subiteration thinning algorithm for extracting medial lines,” *Pattern Recognition Letters*, vol. 19, no. 7, pp. 613–627, 1998, ISSN: 0167-8655. DOI: [10.1016/S0167-8655\(98\)00031-2](https://doi.org/10.1016/S0167-8655(98)00031-2).
- [74] D. H. Douglas and T. K. Peucker, “Algorithms for the reduction of the number of points required to represent a digitized line or its caricature,” in *Classics in Cartography*. John Wiley Sons, Ltd, 2011, ch. 2, pp. 15–28, ISBN: 9780470669488. DOI: <https://doi.org/10.1002/9780470669488.ch2>. eprint: <https://onlinelibrary.wiley.com/doi/pdf/10.1002/9780470669488.ch2>. [Online]. Available: <https://onlinelibrary.wiley.com/doi/abs/10.1002/9780470669488.ch2>.
- [75] A. Griesser and M. Fingerle, “Ai based 3d image analysis with geodict,” *Microscopy and Microanalysis*, vol. 26, no. S2, pp. 518–519, 2020. DOI: [10.1017/S1431927620014920](https://doi.org/10.1017/S1431927620014920).

A. Curriculum Vitae

Education

- 2001-2010** Abitur,
Heinrich-Böll-Gymnasium, Ludwigshafen am Rhein, Germany
- 2010-2014** Bachelor of Science (B. Sc.), Applied Computer Science
University of Kaiserslautern, Germany
- 2014-2016** Master of Science (M. Sc.), Applied Computer Science
University of Kaiserslautern, Germany

Academic and Professional Experience

- 2014-2016** Student assistant
Math2Market GmbH, Kaiserslautern, Germany
- 2016-Present** Software Engineer
Math2Market GmbH, Kaiserslautern, Germany

B. List of Publications

B.1. Core publications

- A. Griebner, R. Westerteiger, E. Glatt, H. Hagen, and A. Wiegmann, “Identification and analysis of fibers in ultra-large micro-ct scans of nonwoven textiles using deep learning,” *The Journal of The Textile Institute*, vol. 114, no. 11, pp. 1647–1657, 2023. DOI: 10.1080/00405000.2022.2145429
- A. Griebner, R. Westerteiger, E. Glatt, H. Hagen, and A. Wiegmann, “Deep learning based segmentation of binder and fibers in gas diffusion layers,” *Next Materials*, vol. 6, p. 100411, 2025. DOI: 10.1016/j.nxmte.2024.100411
- A. Griebner, N. Nunheim, O. Rimmel, A. Blumer, H. Hagen, and A. Wiegmann, “Digital fiber length determination for injection molded glass fiber reinforced composite materials,” in *e-Journal of Nondestructive Testing: 14th Conference on Industrial Computed Tomography (iCT) 2025*, vol. 30, Antwerpen, Belgium, Feb. 2025. DOI: 10.58286/30747

B.2. Further publications

- S. A. Mäkiharju, J. Dewanckele, M. Boone, C. Wagner, and A. Griesser, “Tomographic x-ray particle tracking velocimetry: Proof-of-concept in a creeping flow,” *Experiments in Fluids*, vol. 63, pp. 1–12, 2022. DOI: 10.1007/s00348-021-03362-w
- A. Griebner, M. Hübner, S. Rief, W. De Boever, and L. Hunter, “Metal foams: Linking dynamic ct results to simulation and modeling,” *Microscopy and Microanalysis*, vol. 27, no. S1, pp. 1032–1033, 2021. DOI: 10.1017/S1431927621003901
- M. Weber, A. Griebner, D. Mosbach, E. Glatt, A. Wiegmann, and V. Schmidt, “Copula-based modeling and simulation of 3d systems of curved fibers by isolating intrinsic fiber properties and external effects,” *Scientific Reports*, vol. 13, no. 1, p. 19359, 2023. DOI: 10.1038/s41598-023-46644-5
- M. Weber, A. Griebner, E. Glatt, A. Wiegmann, and V. Schmidt, “Modeling curved fibers by fitting r-vine copulas to their frenet representations,” *Microscopy and Microanalysis*, vol. 29, no. 1, pp. 155–165, 2023. DOI: 10.1093/micmic/ozac030
- M. Weber, A. Griebner, D. Mosbach, E. Glatt, A. Wiegmann, and V. Schmidt, “Investigating microstructure–property relationships of nonwovens by model-based virtual material testing,” *Transport in Porous Media*, vol. 151, no. 6, pp. 1403–1421, 2024. DOI: 10.1007/s11242-024-02079-8
- A. Griebner, R. Westerteiger, C. Wagner, H. Hagen, and A. Wiegmann, “Machine learning-based single fiber extraction from micro-ct scans with geodict,” in *8th Conference on Industrial Computed Tomography (iCT) 2018*, vol. 23, Wels, Austria, Feb. 2018. [Online]. Available: <https://www.ndt.net/?id=21922>

- A. Griebner, R. Westerteiger, C. Wagner, and A. Wiegmann, “Fiberfind: Machine learning-based segmentation and identification of individual fibers in ct images of fibrous media,” in *International Conference on Tomography of Materials & Structures*, 2019
- A. Griesser and M. Fingerle, “Ai based 3d image analysis with geodict,” *Microscopy and Microanalysis*, vol. 26, no. S2, pp. 518–519, 2020. DOI: 10.1017/S1431927620014920
- M. Hümbert, O. Rimmel, and A. Griebner, “Analysis of fibers, pores, and mechanical properties in μ ct-scan of a long fiber-reinforced thermoplastic,” *Microscopy and Microanalysis*, vol. 28, no. S1, pp. 262–264, 2022. DOI: 10.1017/S1431927622001866